HIGH POWER MAGNETRON DESIGN AND ELECTRON EMISSION CHARACTERISTICS

A THESIS SUBMITTED TO
THE GRADUATE SCHOOL OF NATURAL AND APPLIED SCIENCES
OF
MIDDLE EAST TECHNICAL UNIVERSITY

MESUT CEMAL DOĞRU

IN PARTIAL FULFILLMENT OF THE REQUIREMENTS
FOR
THE DEGREE OF MASTER OF SCIENCE
IN
ELECTRICAL AND ELECTRONICS ENGINEERING

JUNE 2018

Approval of the thesis:

HIGH POWER MAGNETRON DESIGN AND ELECTRON EMISSION CHARACTERISTICS

submitted by **MESUT CEMAL DOĞRU** in partial fulfillment of the requirements for the degree of **Master of Science in Electrical and Electronics Engineering Department, Middle East Technical University** by,

Prof. Dr. Halil KALIPÇILAR _____
Dean, Graduate School of **Natural and Applied Sciences**

Prof. Dr. Tolga ÇİLOĞLU _____
Head of Department, **Electrical and Electronics Eng.**

Prof. Dr. Şimşek DEMİR _____
Supervisor,
Electrical and Electronics Eng. Dept., METU

Examining Committee Members:

Prof. Dr. Sencer KOÇ
Electrical and Electronics Engineering Dept., METU _____

Prof. Dr. Şimşek DEMİR
Electrical and Electronics Engineering Dept., METU _____

Assoc. Prof. Dr. Lale ALATAN
Electrical and Electronics Engineering Dept., METU _____

Prof. Dr. Asım Egemen YILMAZ
Electrical and Electronics Eng. Dept., Ankara University _____

Assist. Prof. Dr. Avni AKSOY
Institute of Accelerator Technologies, Ankara University _____

Date: 26/06/2018

I hereby declare that all information in this document has been obtained and presented in accordance with academic rules and ethical conduct. I also declare that, as required by these rules and conduct, I have fully cited and referenced all material and results that are not original to this work.

Name, Last Name: MESUT CEMAL DOĞRU

Signature :

ABSTRACT

HIGH POWER MAGNETRON DESIGN AND ELECTRON EMISSION CHARACTERISTICS

DOĞRU, Mesut Cemal
M.S., Department of Electrical and Electronics Engineering
Supervisor : Prof. Dr. Şimşek DEMİR

June 2018, 84 pages

Microwave applications which requires high power gave raise to need for magnetrons which can generate high power and resist this power. The invention of relativistic magnetrons met that requirment in some extent. However, their inherent pulse-shortening issue limits the obtained energy from that kind of magnetrons. In order to compansate the effects of that problem, the start-up time of magnetrons should be reduced. By this way, the energy in one pulse can be increased. In the literature, there are some methods that hasten the start-up of magnetrons. This work compares some of those methods via simulations that are carried on the relativistic A6 magnetron. In addition, from the results of the simulations an input lumped model for magnetrons is suggested and possible physical implications of that model are explained.

Keywords: Relativistic Magnetron, Fast Start-Up, Transparent Cathode

ÖZ

YÜKSEK GÜÇLÜ MAGNETRON TASARIMI VE ELEKTRON EMİSYON ÖZELLİKLERİ

DOĞRU, Mesut Cemal
Yüksek Lisans, Elektrik ve Elektronik Mühendisliği Bölümü
Tez Yöneticisi : Prof. Dr. Şimşek DEMİR

Haziran 2018 , 84 sayfa

Yüksek güç gerektiren mikrodalga uygulamalar yüksek gücü üretebilen ve bu güce dayanabilen magnetronların tasarlanması ihtiyacını doğurmuştur. Relativistik magnetronların icadı bu ihtiyacı bir ölçüde karşılamıştır. Bununla birlikte bu magnetronların yapısından kaynaklanan darbe kısalması sorunu bu tür magnetronlardan elde edilen enerji miktarını limitlemektedir. Bu problemden kaynaklanan etkileri telafi etmek için magnetronların açılış süreleri düşürülmelidir. Bu yolla bir darbe içindeki enerji miktarı artırılabilir. Literatürde magnetronların açılışını hızlandıran birtakım yöntemler mevcuttur. Bu çalışma bu yöntemleri relativistik A6 magnetronuna uygulanan benzetimler üzerinden karşılaştırmaktadır. Ek olarak benzetim sonuçlarından yola çıkarak magnetronların girişi için bir toplu öğeli devre modeli önerilmekte ve bu modelin olası fiziksel manaları açıklanmaktadır.

Anahtar Kelimeler: Relativistik Magnetron, Hızlı Açılış, Geçirgen Katot

To my family,

ACKNOWLEDGMENTS

In the first place, I would like to express my sincere gratitude to my supervisor Prof. Dr. Şimşek Demir for his excellent supervision. He encouraged me against the feeling that I came to a deadlock and showed me the different points of view for the problem.

I also thank İbrahim Semih Küçük for his help about the simulation program and his comments on my simulations.

I am grateful to Altuğ Altun, Atacan Yağbasan, İsmail Bozkurt and Volkan Öznazlı for their mentorship and help throughout my professional work life. Also, I would like to express my deepest gratitude to my dear colleagues Ali Özgün, Muharrem Keskin and Soner Arıbaş for the warm work environment and for being beyond just a colleague.

I will always be grateful to my dear friend Mehmet Mert Köroğlu. He was with me during hard times and good times. His understanding and support is priceless.

It cannot be enough just an ordinary thank to my mom, Hülya Doğru, and dad, Ahmet Doğru. My gratitude and love to them are inexpressible. I could not even survive without their support and sacrifices. They were always there for me in any conditions.

Above all, I thank my grandma, Emine Akbulut, for her labor on me when I was growing up. That was priceless. I owe to her much.

TABLE OF CONTENTS

LIST OF TABLES

TABLES

LIST OF FIGURES

FIGURES

LIST OF ABBREVIATIONS

3D	Three Dimensional
A-K gap	Anode-Cathode Gap
B-field	Magnetic Field
DC	Direct Current
E-field	Electric Field
EM	Electromagnetic
FDTD	Finite Difference Time Domain
HPM	High Power Microwave
PIC	Particle in Cell
RF	Radio Frequency
TE	Transverse Electric
TWT	Travelling Wave Tube
WG	Waveguide

CHAPTER 1

INTRODUCTION

The magnetron as an oscillator is one of the important sources of the microwave energy. Since its invention, it has been the focus of interest in the microwave society. At the early stages of its existence, it had a great impact on the world history. Utilized as a part of radar systems of that time, it changed the destiny of World War II. Its higher output power in the conditions of that time enabled smaller antennas resulting in compact and efficient radars that can be implemented in planes, ships and land vehicles [1]. Those systems were used extensively during the war and that increased the attraction of magnetrons on the microwave society. As a result more and more studies were carried on magnetrons during the war. However, by the end of the war, new technologies enabling high microwave output power showed up and they took the place of magnetrons and the usage of magnetrons changed into civil applications like microwave ovens. Despite the decreasing usage in military systems, the studies on magnetrons continued in the background and those studies resulted in the relativistic magnetron which is a kind of very high power magnetron. The invention of relativistic magnetrons again attracted attention of the people interested in the high power microwave (HPM) area owing to their high output power in gigawatt levels. Unfortunately, with the invention of those significantly high power relativistic magnetrons, another issue came into question. In spite of their high output power, relativistic magnetrons failed to maintain that output power for long periods and that situation restricted the radiated energy from those magnetrons. That issue was the pulse shortening issue and it was the result of gap closure due to the plasma accumulation in the gap between the anode and the cathode. Therefore, the focus of the researchers on the area

turned towards an investigation on finding a solution for that issue or at least a way compensating the effects of the problem. One way found for the compensation was reducing the start-up time of the magnetron. In that way, it was aimed to increase the time of the magnetron operation in a pulse duration and to increase energy per pulse, i.e., to enhance average output power, as a result. Since then, researches have been carried out in order to improve the magnetron start-up and to reduce the time elapsing during the start. Today, there are several methods that speed up the start of magnetrons. In this thesis work, those methods were investigated via particle-in-cell (PIC) simulations. In addition, a basic lumped element model was developed in order to explain the transient behavior of the magnetron start-up. Based on those investigations, the thesis consists of five chapters following the introduction. In the second chapter, an overview for the magnetron concept is given in terms of what a magnetron is, how it operates, which parameters are concerned while the design process and which output parameters are examined in order to test the performance. Also, there are a brief history of magnetrons and a definition for the relativistic magnetron, which is the type of magnetron investigated throughout the thesis, in that chapter. The third chapter comprises the literature search results on the fast start-up techniques for magnetrons such as the priming techniques and the transparent cathode concept. The simulation work that carried out on those techniques are mentioned including the simulation model and the results in the fourth chapter after a brief description of the simulation environment and the magnetron (A6 magnetron) used in the simulations. In the fifth chapter, the developed input lumped model for magnetrons is explained besides the possible physical implications of that model. Finally, at the last chapter, the results of the thesis work are evaluated as a conclusion.

CHAPTER 2

MAGNETRON STRUCTURE AND OPERATIONAL PRINCIPLES

2.1 Magnetron and Its Structure

Magnetron is a vacuum tube oscillator which utilizes crossed electric and magnetic fields in order to generate microwave signals. Among other high power microwave sources, it is the self-excited one, which means oscillations starts in its own resonators without the requirement for an external signal to be amplified. In this sense, it differs from the high power microwave sources like klystrons, TWTs etc. Collins defines a magnetron as an EM wave-producing diode by the means of a magnetic field [2]. A magnetron is a diode because of its structure consisting of an anode-cathode pair confining electrons in between. A typical magnetron structure can be seen in Figure 2.1. Primary elements are a cathode retained at negative potential, an anode block, which is potentially grounded, and a space between them called the interaction space. The cathode is the source of electrons in a magnetron through an emission process which could vary from one to another type of magnetrons. Besides of providing, together with the cathode, the required electric field for the motion of the electrons in the interaction space, the anode block is the unit where microwave oscillations take place due to resonators on it. As a self-excited oscillator, a magnetron generates RF or microwave output by transforming DC input in the interaction space where the electrons transfer their energy, which they take from DC input, to the RF or microwave oscillations in the resonators. Also, a constant magnetic field, which helps the formation of the desired trace of the electrons in the interaction space, is kept in the interaction space uniformly and axially [2]. Apart from these main

elements, there are some other elements which could be optional. One of them is the heater in the cathode structure. That heater is necessary in conventional magnetrons, in which thermionic emission process occurs, in order to remove electrons from cathode while it is not necessary in relativistic magnetrons. The other one is the coupling coaxial RF probe used for the extraction of the output power. Instead of that probe, other coupling means can be used such as a coupling loop or a waveguide aperture. Another one is the straps. They can be inserted on the anode block in order to facilitate the formation of the desired mode of the magnetron. There is also a structure supplying the required magnetic field in the magnetron. It can be a permanent magnet or a coil structure.

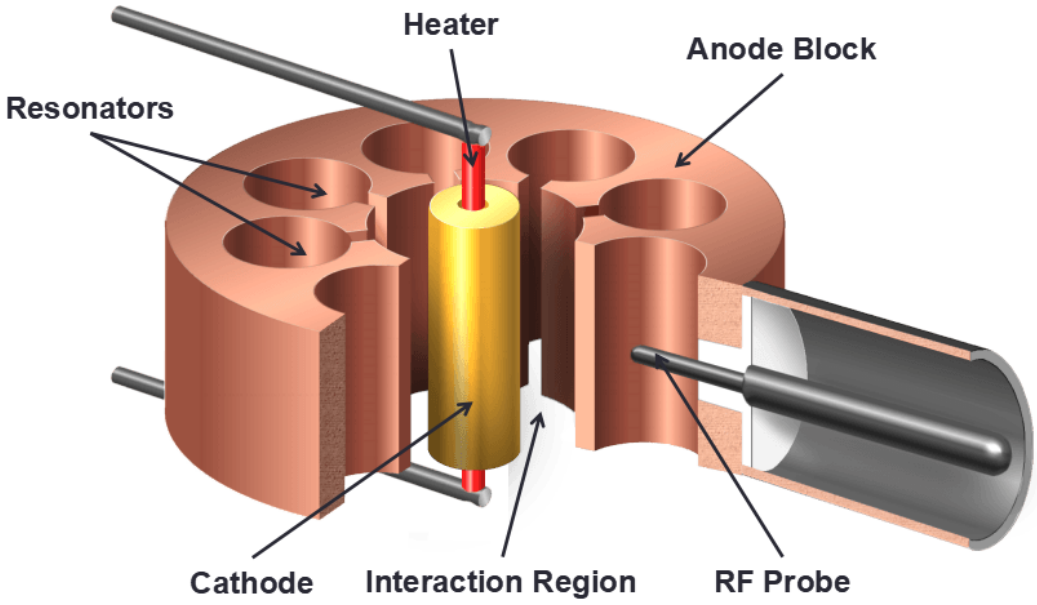

Figure 2.1: A typical structure of a magnetron [3]

2.2 Operation of a Magnetron

Basic magnetron operation goes through the following processes. It starts with the emission of the electrons when magnetron is powered up. It continues with the formation of an electron cloud around the cathode under the DC electric

and magnetic fields. Formation of the electron spokes under the influence of RF fields in the cavities follows the electron cloud. Finally, energy transfer between the electrons in the spokes and RF fields in the cavities takes places and RF oscillations grows up to a saturated power. Those oscillations go on until magnetron is powered down.

In order to understand how the electron cloud arises, it is convenient to treat the process in a single electron point of view. An emitted electron from the cathode moves in the interaction region under the influence of Lorentz force,

$$\vec{F} = q\vec{E} + q(\vec{v} \times \vec{B}) \tag{2.1}$$

where q is the electron charge, $\vec{E}$ is the radial E-field, $\vec{v}$ is the electron velocity and $\vec{B}$ is the axial B-field. That electron follows a trace as in Figure 2.2. That

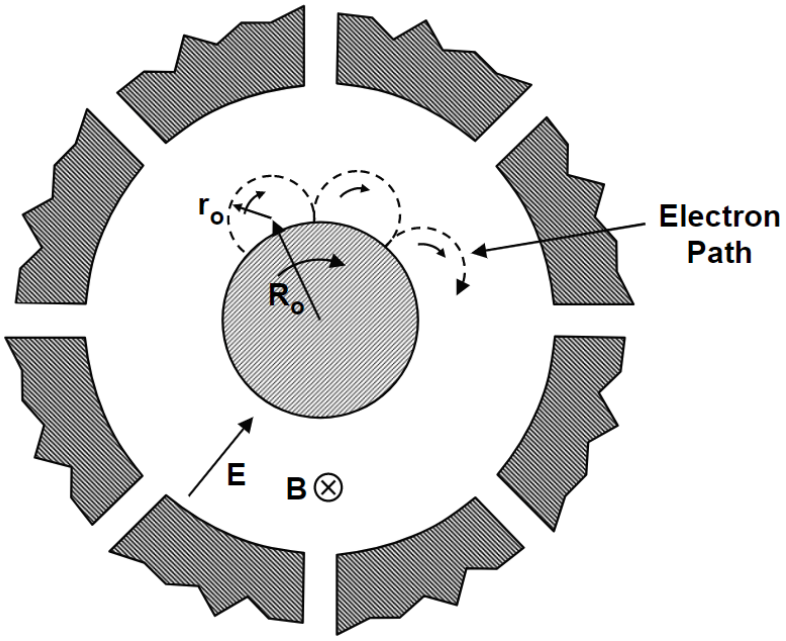

Figure 2.2: Path of the electron under the influence of Lorentz force [4]

trace is such that there is a rotation around the cathode (R_0) which is slow and there is another rotation with a small radius (r_0) which is fast and the total of both rotations is the electron trace [4]. Changing single electron point of view to all electrons emitted from the cathode, the electrons form two type of steady state stream. One is double-stream state, which consists of orbits intersecting the cathode, and single-stream state, also named Brillouin stream, which consists

of circular orbits around the cathode [5]. The former one corresponds to the fast rotation trace of the single electron and the latter corresponds to slow rotation of the single electron. As a result of those streams, an electron cloud as in Figure 2.3 is formed. That cloud has some thickness from the cathode and

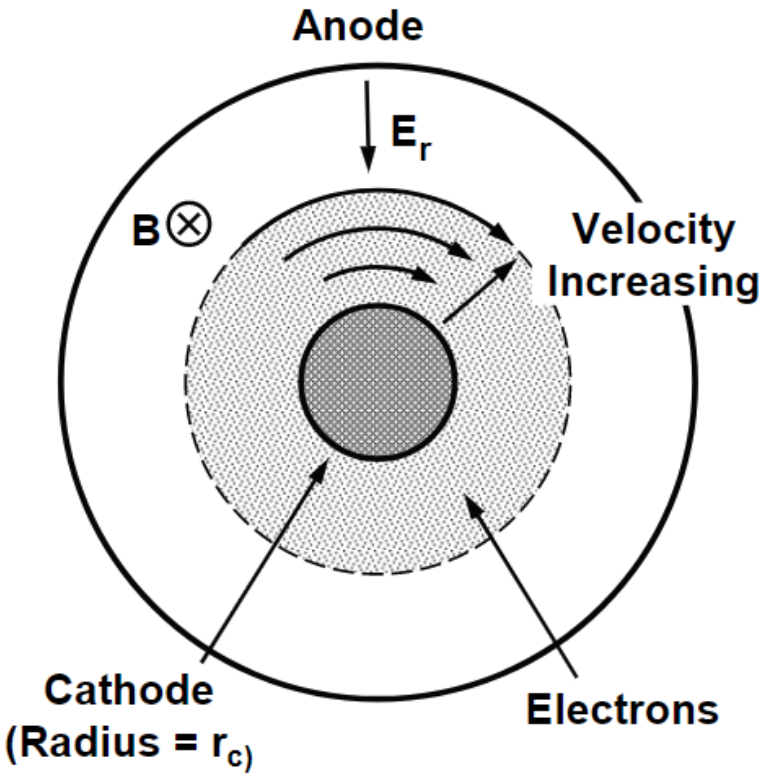

Figure 2.3: Electron cloud formed at the start-up of a magnetron [4]

electrons in the cloud rotates under the effect of electric and magnetic fields with a drift velocity [6],

$$\vec{v_d} = \frac{\vec{E} \times \vec{B}}{|B|^2} \tag{2.2}$$

Due to the space charge and diamagnetic effects caused from the electron cloud, electric and magnetic fields changes from cathode to the end of the thickness of the cloud. Therefore, drift velocity of the cloud, v_d, also changes [6]. In fact, that change is in the manner that v_d increases as distance from the cathode increases.

Current due to the rotating electrons in the electron cloud has a noisy component on itself because of the randomness of the electron density and the electron

velocity in the cloud. That noise can be classified as a white noise consisting of infinite frequency range in the spectrum [4]. That is the force which starts the RF oscillations in the cavities of the magnetron. Since the cavities have band-pass characteristics, only frequency components of white noise that the cavities support can grow up. After the initiation of the RF fields in the cavities, those fields interacts with the electron cloud in the interaction space. Interaction between the electrons in the cloud and the RF fields can be seen in Figure 2.4.

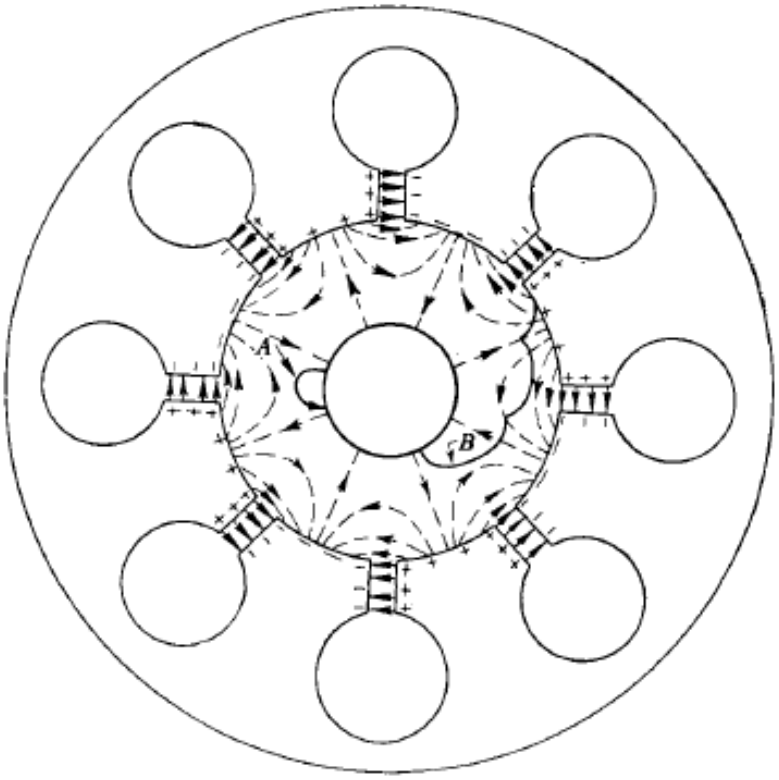

Figure 2.4: Interaction between RF fields and electrons in the A-K gap [2]

Electrons in a region where RF electric fields promote their rotation , such as A in Figure 2.4, are accelerated by the RF fields and because of the increase in the velocity, the path of the electrons is bent towards the cathode under the influence of Lorentz force due to DC fields. On the other hand, the electrons in a region where RF electric fields oppose their rotation, as B, the electrons are decelerated and they close to anode [2]. Those interactions end up with the spokes as in Figure 2.5. Those electron cloud structure with spokes rotates around the

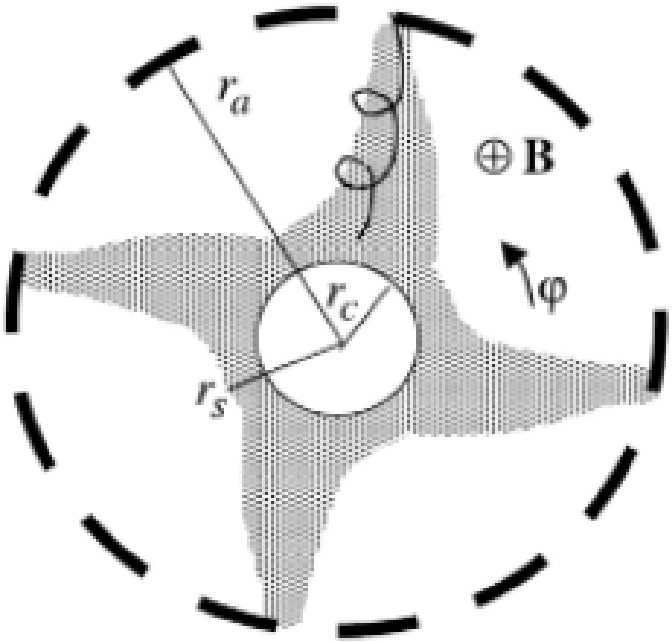

Figure 2.5: Electron spokes [5]

cathode with the drift velocity in (2.2) because of the RF fields in the cavities alternate with a period of the RF oscillations. A synchronism between the RF fields and the rotation of the cloud with spokes occurs, i.e., drift velocity, v_d, of electrons become equal to the phase velocity of the oscillations at which phase of the RF field rotates around the anode structure. In this case, decelerated electrons transfer their energy to the RF oscillations and the oscillations grow up to their saturated power. That transfer continues during the operation of the magnetron.

2.3 Magnetron Design Parameters

There are several physical and input parameters when designing a magnetron. In their book, Benford et al. outline the main parameters to be considered when designing a magnetron as the cathode, which determines the electron emission characteristics, the interaction region, which affects the formation of electron cloud and spokes, the anode and the cavity structure, which determines the mode and the frequency of the magnetron, and the axial DC magnetic field,

whose strength determines whether the magnetron conducts or is in cut-off or operates as a magnetron [6]. In general, parameters such as radial electric field, axial magnetic field, resonator dimension, number of resonators and A-K gap dimension have to be considered in the design process. First two are input parameters to the magnetron from the external sources and the others are related to the physical dimension of the magnetron structure.

2.3.1 Input DC Fields

Input voltage to the magnetron, which corresponds to the radial E-field, and the axial B-field determine the path which electrons move in the interaction region. For a given input voltage, electron paths with respect to different B-field values are given in Figure 2.6. If there is no B-field, electrons will not be deflected and

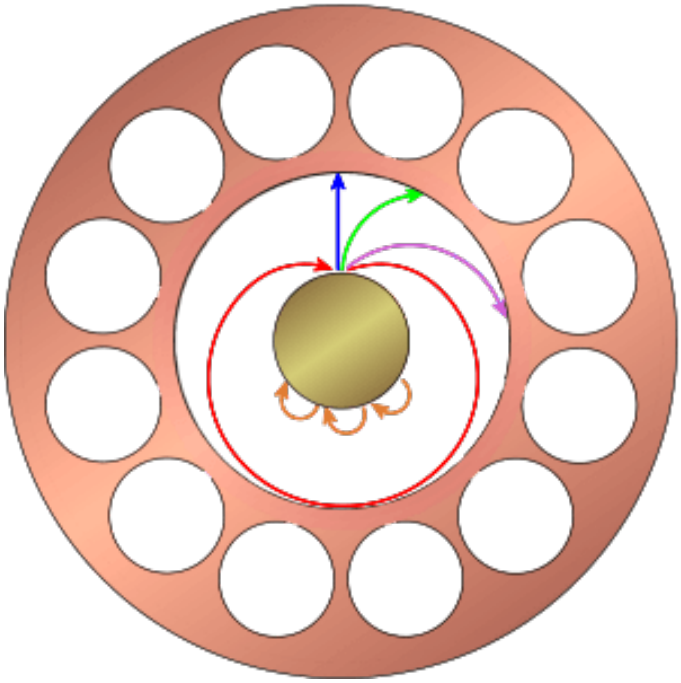

Figure 2.6: Electron paths for different B-field values [3]

goes directly to the anode as in blue trace. Applied B-field deflects the electrons as in green trace. As strength of the B-field is increased, electrons are deflected more like purple trace. Continuing to increase the strength, electrons just touch the anode and return back as in red trace at some point. That point is called

Hull cut-off [3]. That minimum B-field value that prevents the magnetron to conduct as pure diode is calculated using [6],

$$B^* = \frac{mc}{ed_e}\left[\left(\frac{2eV}{mc^2}\right) + \left(\frac{eV}{mc^2}\right)^2\right]^{\frac{1}{2}} \tag{2.3}$$

where m is the electron mass, e is the electron charge, c is the speed of light, V is the A-K gap voltage and d_e is the effective gap. Effective gap is given by [6],

$$d_e = \frac{{r_a}^2 - {r_c}^2}{2r_a} \tag{2.4}$$

where r_a is the anode radius and r_c is the cathode radius. Increasing further the B-field from the Hull cut-off value, the magnetron operates in normal operation. However, that increase is not unlimited. After some point, the interaction between RF fields and the electrons breaks as in orange trace of Figure 2.6 because the electrons become too slow to synchronize with the phase velocity of RF fields. That value at which the magnetron switches from the normal operation to the cut-off state is named as Buneman-Hartree condition given by [6],

$$\frac{eV}{mc^2} = \frac{eB_z\omega_n}{mc^2 n} r_a d_e - 1 + \sqrt{1 - \left(\frac{r_a\omega_n}{cn}\right)^2} \tag{2.5}$$

where n is the mode number, ω_n is the angular frequency of the mode and B_z is the axial magnetic field. Other parameters in (2.5) are the same as in (2.3) and in (2.4). In summary, for a given radial E-field, axial B-field has a lower limit, which is Hull cut-off, and an upper limit, which is Buneman-Hartree condition, in order the magnetron to operate normally. Those limits and the magnetron operation regions can be shown in Figure 2.7. When choosing input voltage and axial B-field in the magnetron design, it could be efficient to put the operation point to just left of Buneman-Hartree curve [6].

2.3.2 Physical Dimensions

Physical dimensions of the cavities on the anode and the number of them determines the mode at which the magnetron operates. Due to the closed structure of the resonator system in the magnetron, the total phase shift in one turn around the magnetron has to be the integer multiple of 2π [2]. Therefore, the phase

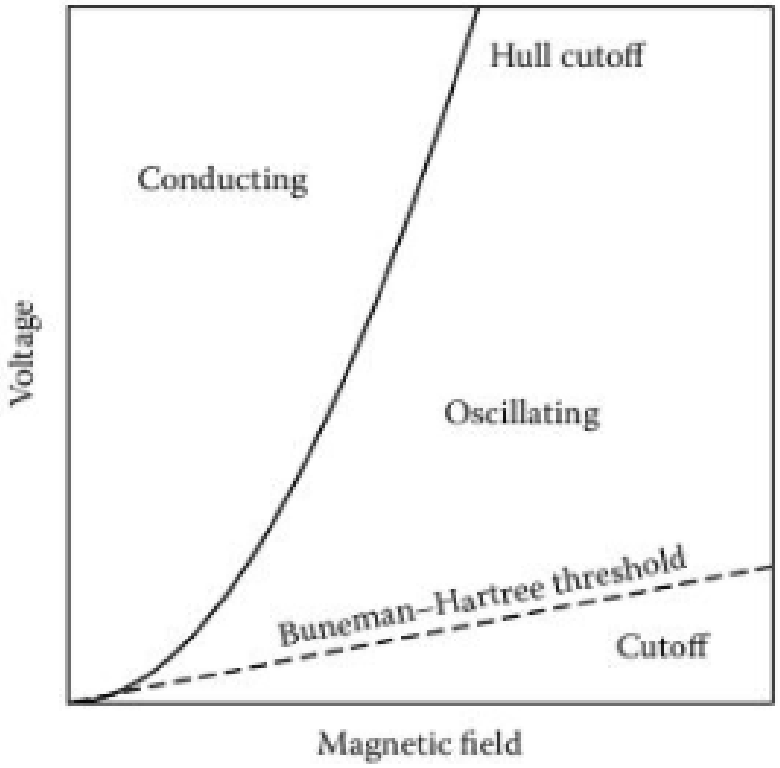

Figure 2.7: Magnetron operation regions and limiting curves [6]

shift between the two neighboring resonators is as [6],

$$\Delta\theta = \frac{2\pi n}{N} \qquad n = 1, 2, ..., \frac{N}{2} \tag{2.6}$$

where n is the mode number and N is the number of the cavities. A relation which relates that phase shift to the operating frequency of a mode is the dispersion relation. A typical dispersion diagram can be seen in Figure 2.8. In the figure lower curve shows the lowest order modes and the upper curve shows the next higher order modes. Benford et al. suggest an approximate equation which relates the radial size of the cavity to the frequency of the π-mode operation of a magnetron. That equation is [6],

$$f_\pi = \frac{c}{4(r_v - r_a)} \tag{2.7}$$

where c is the speed of light, r_a is the anode radius and r_v is the radius at the end of the vanes. Equation (2.7) shows that there is a inverse relation between the cavity size and the frequency of the magnetron. That equation can be used

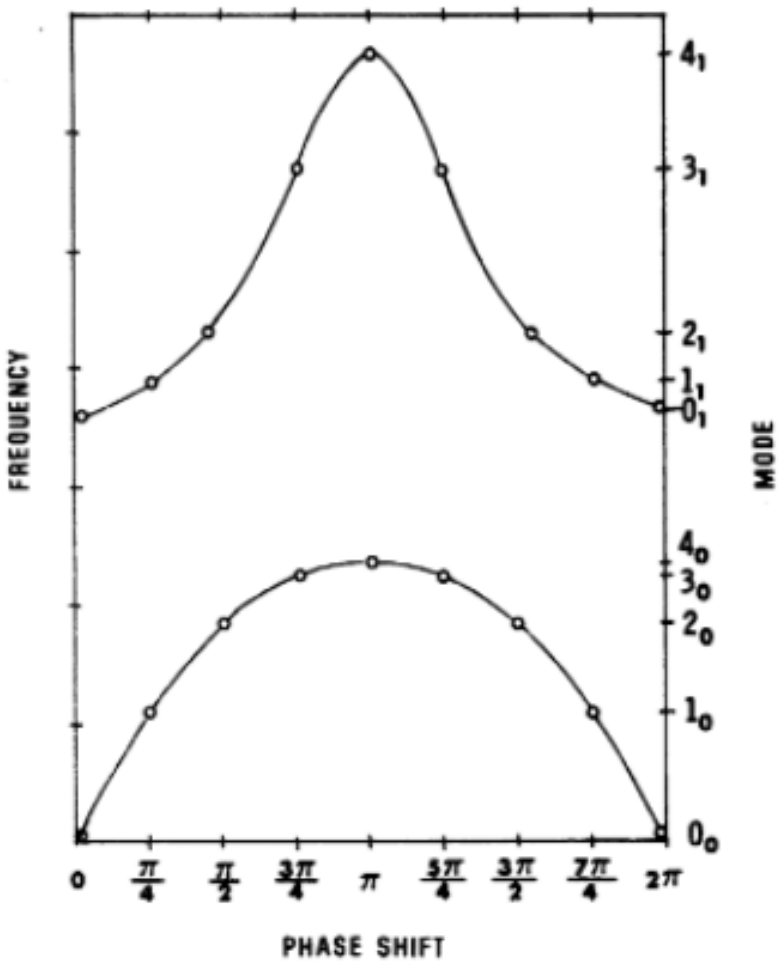

Figure 2.8: Dispersion diagram for a magnetron having 8 cavities [7]

when determining the frequency in the design process. The effect of the axial modes on frequency is as [6],

$$\left(f_n{}^g\right)^2 = \left(f_n{}^0\right)^2 + \left(\frac{gc}{4h}\right)^2 \qquad g = 1, 2, 3, ... \tag{2.8}$$

where $f_n{}^0$ is the frequency when there is no axial mode effect, c is the speed of light, g is the axial mode number and h is the axial length of the cavities. In Equation (2.8), it can be seen that second term of the equation gets smaller when axial length of the cavities increases and the mode separation decreases. That can result in mode competition [6]. Therefore, it is important not to set the axial length too long when designing a magnetron.

2.4 Magnetron Output Parameters

When designing a magnetron or choosing the suitable magnetron for an application, the basic parameters one has to consider are the frequency, the output power and the efficiency. Those three output parameters can be shown in performance charts with respect to input values as given in Figure 2.9. The

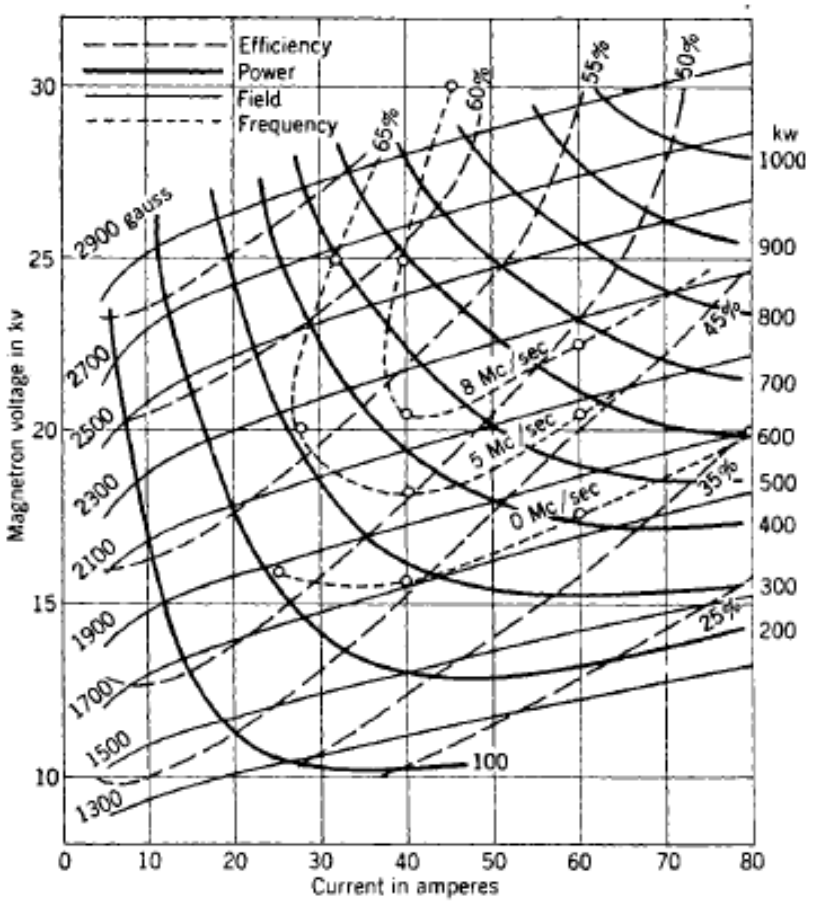

Figure 2.9: A performance chart for a magnetron [2]

frequency of the magnetron is related to the excited mode in the cavities of the magnetron. That mode is determined by the dimension of the cavities and also the applied fields. If those values are not arranged properly, a mode competition issue can occur. Therefore, observing the output frequency spectrum with respect to applied field values is important. As another output parameter, the output power is required to be high because with the higher output power is, the HPM systems are more effective. For example, the maximum range of a

radar system increases with the increasing output power. The mode competition issue in frequency spectrum also causes the decrease in the output power and the efficiency. The efficiency is the ratio between the output RF power and the input DC power. It is related to the matching of the input structure and the output structure. It also depends on the electron motion in the interaction space. Besides those parameters, the start-up time of a magnetron can be investigated as another parameter of the magnetron. It is critical especially for short-pulse applications. Some studies have been carried out for some time now in order to improve the start-up process of a magnetron and speed up the start of the magnetron. Those studies will be mentioned in the following chapters.

2.5 Historical Development of Magnetron

The magnetron appeared first time in the history with Hull's study on the electron motion between concentric cylinders under the influence of a magnetic field during his quest to find an alternative of Lee de Forest's triode structure. In 1921, he published those studies which formed the basis of the magnetron in [8] and that structure was noted as the first magnetron although it was not used as an oscillator. The utilization of that kind of structure as an oscillator was realized by August Žáček and Erich Habann in the same year, 1924, but independently. Žáček's magnetron oscillator was similar to the structure that Hull used in the studies. On the other hand, Habann's magnetron had a split-anode consisting of two parts and producing a negative resistance. At the end of 1920s, Kinjiro Okabe carried out the significant study on that split-anode magnetron and that study was given in [9] by Hidetsugu Yagi in 1928. In 1930s, magnetron studies were carried out in Europe. During those studies, starting from the split-anode structure having two segments on it, magnetrons with multi-segment anode structures were developed. One of those multi-segment magnetrons was Klaas Posthumus's magnetron having four segments. He also explained the theory behind the generation of the oscillations which was the rotating field oscillations. That work [10] was the first one which clearly showed the operation of the magnetron and the generation of the oscillations through the energy transfer

between the synchronized field and the rotating electron cloud. Following those developments, the multi-cavity magnetron having cavities on the anode showed up. Arthur Samuel came up with one of that kind of magnetron and patented it [11] in 1936 but his work stayed theoretical. Another patent [12] describing a multi-cavity magnetron was written by Hans Erich Hollmann in 1938. A very successful one of multi-cavity magnetrons was designed by Alekseev and Malairov in the same years with the other ones and they tested the design with experiment. They published their work in 1944 [13]. In 1939, when they were unaware of the previous works on the multi-cavity magnetron, Boot and Randall came with an idea to construct a multi-cavity magnetron and they constructed it in 1940. They tested that magnetron in a radar in the same year and the results were very successful. Although there were previous works on the cavity magnetron, Boot and Randall were credited as the inventors of the cavity magnetron. Their design formed the basis of today's magnetrons which are the type of the cavity magnetron. They described their design in a paper [14] in 1946. Later, Megaw, who was also carried out studies on multi-cavity magnetrons in 1930s and had patents on that topic, helped the improvement of their design and he wrote a paper [15] describing early developments in magnetron design in 1946. Boot and Randall took out a patent for their magnetron design in 1951 [16] and for improved one in 1953 [17]. That design was used in radar systems during World War II and had great impact on the war. After the war, the studies on the radar systems were focused on the other microwave sources and the usage of magnetrons changed into commercial applications, especially microwave ovens after 1958. During that time, studies on the magnetrons continued and some improvements were done. However, magnetrons became an attractive high power microwave (HPM) source again for the military electronic warfare applications with the invention of the relativistic magnetron by Bekefi and Orzechowski in 1976 because that magnetron structure enabled higher output powers from a magnetron. They described their relativistic magnetron structure in [18]. The studies after the invention of the relativistic magnetron focused on improving the pulse duration and the efficiency of the relativistic magnetron structure. In order to achieve that purpose, studies were carried out on fast start-up techniques in 2000s. Those techniques include the priming techniques and the transparent

cathode structure. A description of the relativistic magnetron will be given in next section and the fast start-up techniques will be explained in next chapter.

2.6 Relativistic Magnetrons

A relativistic magnetron is a magnetron type which enables very high power outputs. The structure of a relativistic magnetron is very similar to a conventional one. Those magnetrons are separated by only two aspects. The first one is that the voltage and the current which drive the magnetron are larger in relativistic magnetron. Since the kinetic energy achieved by the electrons is comparable to the rest mass energy of an electron ($m_e c^2 = 511$ keV) with these voltages, it is called as relativistic. The second one is the way that the electrons are emitted is different for both magnetrons. The conventional magnetron emits the electrons by using a hot cathode. On the other hand, the relativistic one uses very high E-field in order the electrons to be emitted from a cold cathode. That results in the production of very large current densities making very high power microwave possible [19]. In his paper, Benford makes comparison between conventional and relativistic magnetrons. That comparison can be seen in Table 2.1 [20]. Inves-

Table2.1: A comparison between conventional and relativistic magnetrons [20]

PARAMETER	CONVENTIONAL	RELATIVISTIC
Voltage	$\leq$100 kV	$\geq$500 kV
Current	$\sim$100 A	$\geq$5-10 kA
Emission	Thermionic	Explosive
Pulse Duration	$\sim$1 ms	$\sim$100 ns
Rise Time	$\leq$200 kV/ms	$\sim$100 kV/ns
Peak Power	$\leq$10 MW	$\sim$1 GW
Efficiency	$\sim$50%	$\sim$20-40%
Tunable Range	$\sim$5%	$\sim$30%

tigating the table, it is obvious that the relativistic magnetron has much higher output power than the conventional one. However, the relativistic magnetron falls behind the conventional one in the pulse duration aspect. Because of the short pulse duration, the energy radiated at the output of relativistic magnetrons

is limited even though they have very high output power. That situation is the pulse-shortening issue in relativistic magnetrons. Actually, the pulse-shortening issue exists in all HPM devices due to effects of the plasma formed in them. In [21], the reasons why the pulse-shortening occurs in HPM devices and what the plasma causes are explained in detail. In relativistic magnetrons, the plasma exists around the cathode and that plasma expands with time. That is the closure of the A-K gap. It makes the same effect as the increased cathode radius. With the input voltage remaining unchanged, the decrease in the gap between the anode and the cathode structures results in the increase of E-field on the electrons in the interaction space and the increase of the rotating speed of the electrons according to Equation (2.2). In order the magnetron operates properly, the azimuthal drift velocity of the electrons and the phase velocity of the microwave oscillations in the cavities have to be in synchronism. The increase of the azimuthal drift velocity of the electrons disturbs that synchronism. As a result, the frequency of the oscillations shifts in order to increase the phase velocity and catch the drift velocity. As time elapses, the plasma expands more and more and the drift velocity increases further. The change of the mode of the oscillations in order to keep the synchronism follows that increase. That continues until the synchronism is lost eventually and the magnetron operation ends [22]. As a conclusion, it can be said that there is a maximum time until which the magnetron can operate due to the gap closure caused by plasma and that limit the maximum pulse duration in relativistic magnetrons. In order to increase the radiated energy which is limited due to the pulse-shortening, the start-up time of the magnetron have to be decreased. In that way, the time in which the magnetron supplies output power in one pulse duration is increased and one pulse duration is used more effectively. The following chapters searches the ways which hastens the start-up of magnetrons.

CHAPTER 3

TECHNIQUES FOR FAST START-UP IN MAGNETRONS

The society interested in magnetrons as a HPM source has been in quest of the ways that enhance the output power of magnetrons, especially relativistic ones. However, that magnetrons have two problems preventing that enhancement. One of them is the pulse shortening and the other one is the low efficiency [23]. Therefore, in order to increase the output power, it is required to solve the pulse shortening issue and increase the efficiency at the same time. The pulse shortening issue can be solved by reducing the time required to start the magnetron, i.e., the start-up time of the magnetron. In this way, the time that the magnetron operates in a pulse would be increased. That implies an increase in the energy per pulse which raises the average output power. The start-up time could be improved by decreasing the A-K gap width or increasing the width of the electron cloud by changing the DC E-field and the DC B-field because the interaction and the power transfer between the electrons and the oscillations advance when the electrons come closer to the anode. Unfortunately, that closeness causes the efficiency to decrease due to the fact that the number of the electrons that hit to the anode increases [24]. That situation is contradictory to the purpose of an improvement in both the start-up time and the efficiency. In that case, a requirement for new methods arises. In their paper, Bosman et al. define the factors that affect the start-up time as follows [25]:

- The start conditions
- The rate of build-up

The start conditions are determined by the initial noise. It causes the instabil-

ities in the electron cloud that provide the formation of the electron bunches, or the spokes, of the operating mode. However, that formation from the initial noise is too slow [25]. Also, during that formation process, a mode competition issue can occur. That results in the disruption of the start-up process of the desired mode [26] and causes even a slower start-up. There are several techniques which was developed in order to improve the start conditions and make the start-up faster while decreasing the mode competition. Those techniques are called as priming techniques. Andreev and Hendricks list those priming techniques in their paper as follows [24]:

1. Cathode priming
2. Magnetic priming
3. Anode priming
4. RF priming

The rate of build-up depends on the tangential RF E-field at the end of the electron cloud in the interaction space [25]. That E-field can be changed in order to improve the rate of build-up by using a shaped cathode. That shaped cathode could be a transparent cathode described in [27] or a semi-transparent one as in [28].

3.1 Priming Techniques

The priming in the magnetrons can be defined as the excitation of the desired operating mode by choice using some external means. Jones et al. list some purposes of the priming as such [29]:

- Faster start-up of oscillations
- Elimination of the mode competition
- Frequency locking

In the following sections, some of such external means by which those purposes are realized will be explained via the studies in the literature.

3.1.1 Cathode Priming

In the cathode priming technique, the cathode of the magnetron is arranged such that only some discrete regions of the cathode, which are aligned in a periodic order in azimuth, emit electrons and between those regions there are non-emitting regions. That results in a formation of azimuthally periodic electron bunches, as in Figure 3.1, around the cathode with the start of the emission. That modulated structure of the electrons in the A-K gap implies the simultaneous start of the RF current with the emission as opposed to the case of ordinary cathode in which the RF current starts after the formation of the electron cloud with the help of the noise by a slow process. The energy transfer between the electrons and the oscillations occurs as soon as the Buneman-Hartree threshold is passed by the applied voltage. As a result, the cathode priming provide the fast start-up by the faster formation of RF current in the electron cloud [25].

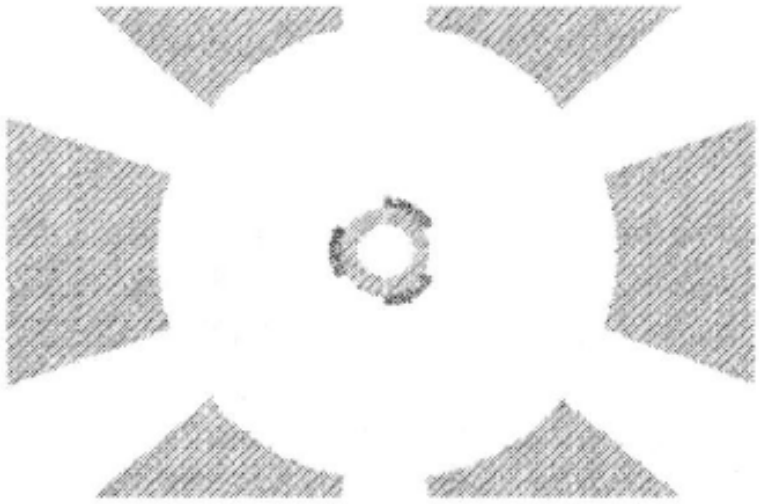

Figure 3.1: Electron bunches at the start of the emission in the cathode priming technique [30]

The emitting regions on the cathode are arranged in a way that supports the desired operating mode of the magnetron and thus eliminating the mode competi-

tion. For example, in Figure 3.1, there are three emitting regions on the cathode surface and they are placed under the vanes. That forms a three-fold electron bunch structure which supports the formation of the spokes in the π-mode operation of that six cavity magnetron. In their paper Jones et al. simulates that six cavity magnetron with emitting regions arranged as stated and compare the formation of the electron spokes as in Figure 3.2. At t=7.363 ns, the electron

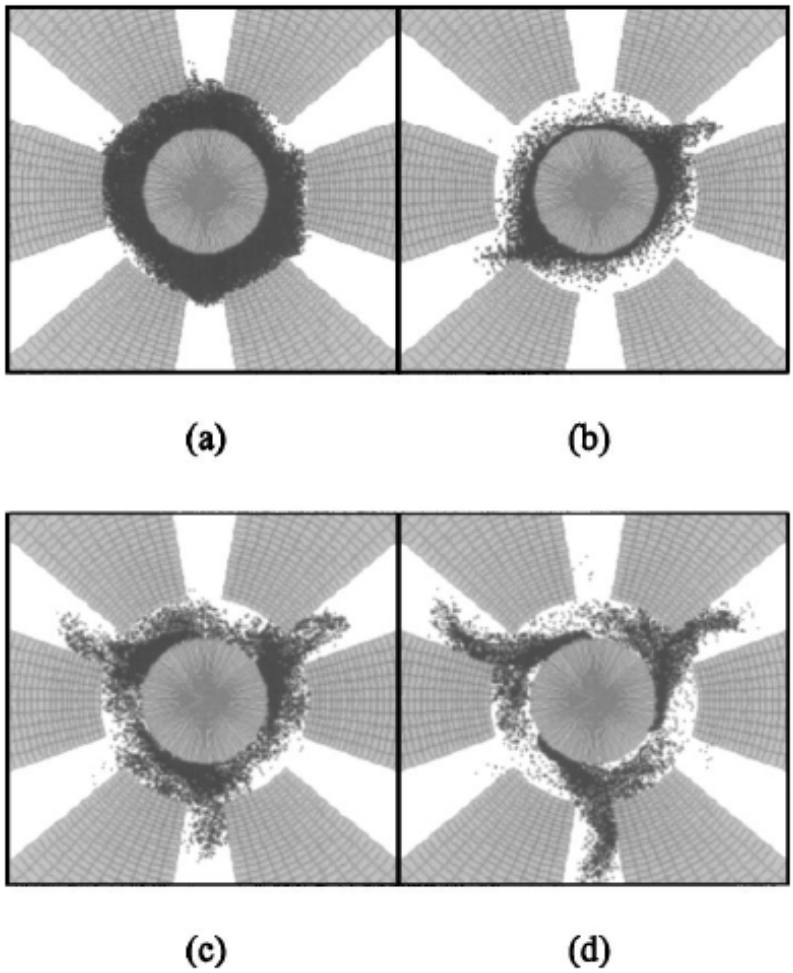

Figure 3.2: Comparison of electron spoke formation with and without cathode priming: (a) t=7.363 ns without cathode priming, (b) t=13.413 ns without cathode priming, (c) t=7.363 ns with cathode priming and (d) t=13.413 ns with cathode priming [29]

spokes of the desired π-mode are formed in the structure with cathode priming while there exists a uniform electron cloud in the one without cathode priming. Also, at t=13.413 ns, the electron spokes continues in the structure with cathode

priming while the electron spokes of another mode ($2\pi/3$) are formed in the one without cathode priming [29].

They also give the output frequency plot with respect to time as in Figure 3.3. That figure shows that the frequency of the oscillations becomes stable at around 13 ns in the structure with cathode priming; on the other hand, the frequency of the oscillations becomes stable at around 30 ns after the frequencies of the other modes show up [29].

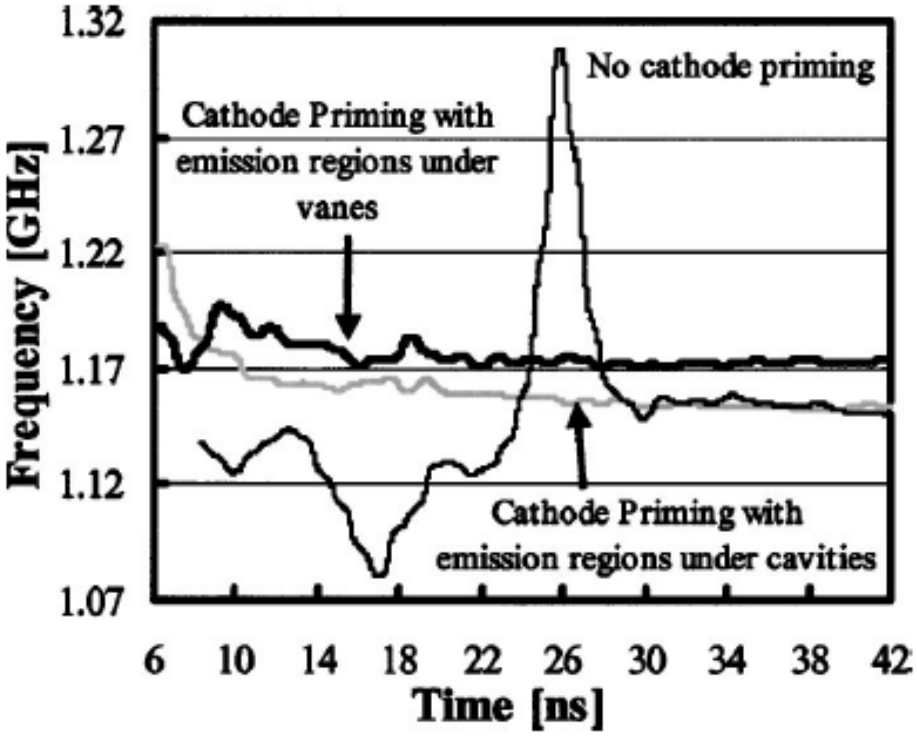

Figure 3.3: Comparison of the instantaneous output frequency with and without cathode priming [29]

In another paper, they experimentally measure the output power of the same structure as in simulation. Figure 3.4 shows the results. With the same applied voltage, it is obvious that microwaves start 180 ns earlier in the structure with cathode priming [30].

Investigating the simulated data in [29] and experimental data in [30], it can be concluded that the cathode priming makes the start-up faster in addition to eliminating the mode competition.

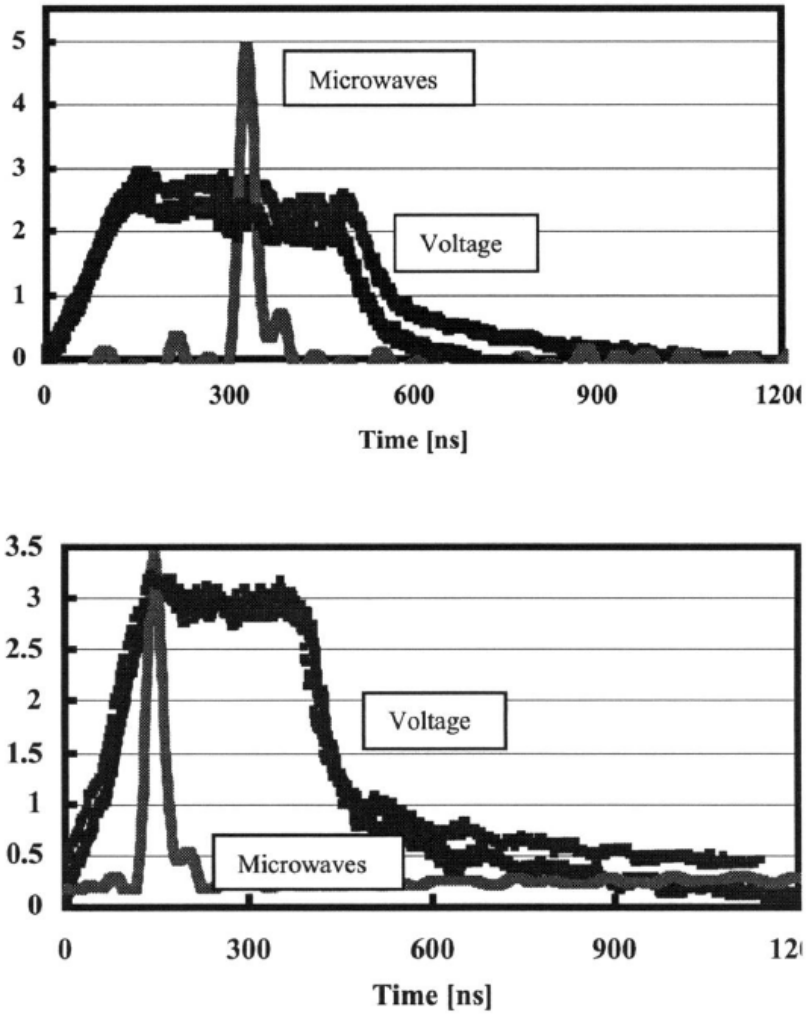

Figure 3.4: Comparison of the instantaneous output power with (bottom) and without (top) cathode priming [30]

3.1.2 Magnetic Priming

The magnetic priming is a technique which utilizes the DC B-field in order to pre-bunch the electrons in the A-K gap in favor of the desired operating mode; hence, eliminates the mode competition and speeds up the start-up. In that technique, the DC B-field is modulated in azimuthal direction and in a periodic manner [31]. The azimuthally modulated B-field causes the electrons in the electron cloud to form bunches arranged in an azimuthally periodic manner around the cathode due to the effect of Lorentz force in (2.1). That helps the formation of the spokes of the desired operating mode and eliminates the requirement of an

initial noise for the formation of the RF current in the electron cloud; therefore, the start-up becomes faster.

Neculaes et al. realize the magnetic priming technique in their paper by placing permanent magnets periodically around the magnetron's original magnet. This structure can be seen in Figure 3.5. The magnetron in the structure has ten cavities on the anode; thus, five magnets are placed periodically around the structure in order to support the formation of five spokes of the desired π-mode.

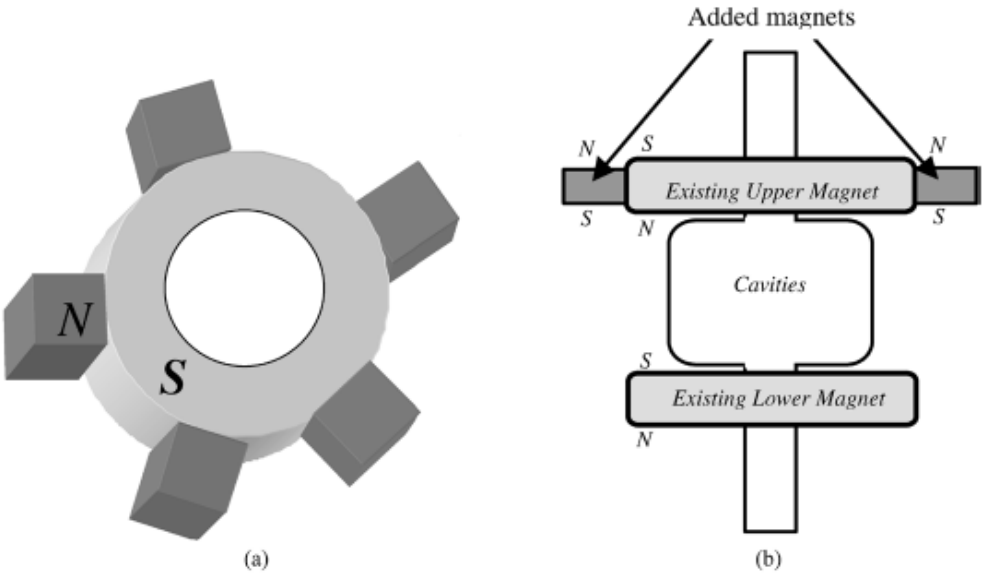

Figure 3.5: Magnetron structure with magnetic priming : (a) Top view of the structure and (b) Side view of the structure [32]

They simulate that structure and compare the output power graphs with and without magnetic priming as in Figure 3.6. In those graphs, the time at which the output power of the magnetron reaches steady-state is 40 ns with magnetic priming while it is 70 ns without magnetic priming [32].

In another paper, they simulate a six-cavity relativistic magnetron. In the simulation, in order to simulate the effect of the periodically arranged magnets, they apply the axial magnetic field as [31],

$$B_z(\theta) = B_0\big[1 + \frac{\alpha}{2} sin(3\theta)\big] \tag{3.1}$$

where B_0 is the base magnetic field and α is the magnetic priming strength.

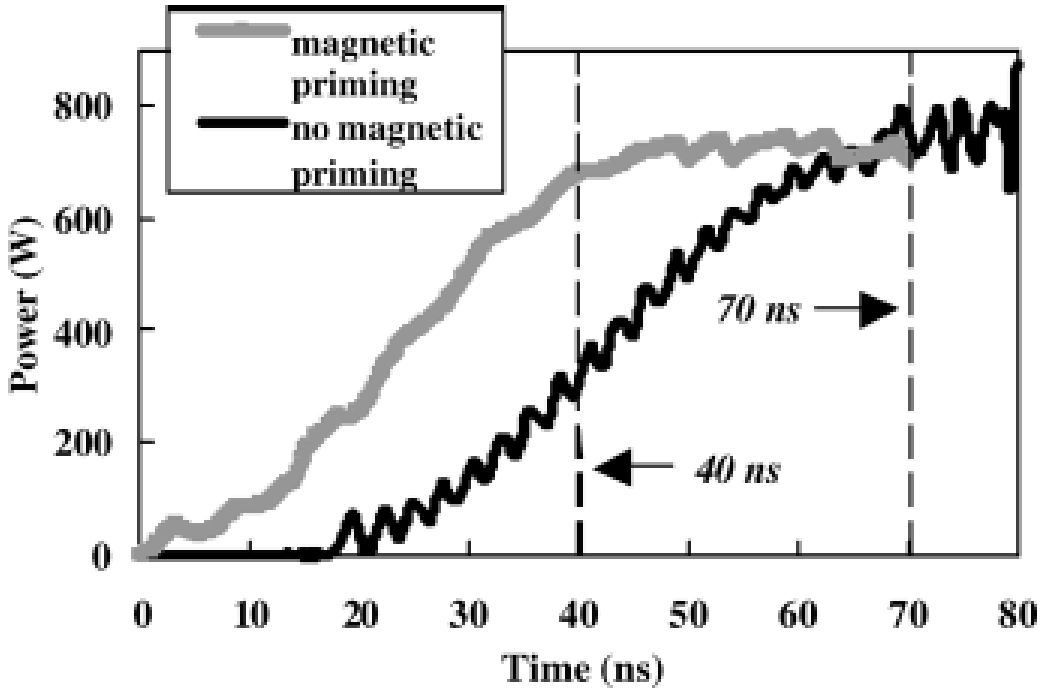

Figure 3.6: Comparison of the instantaneous output power with and without magnetic priming [32]

They show the evolution of the spokes in the simulation with and without magnetic priming as in Figure 3.7. At 13.536 ns, the spoke structure of the desired π-mode is already formed with magnetic priming while there is only an electron cloud without magnetic priming. At another time step t=17.345, the spokes continue to exist in A-K gap with magnetic priming; on the other hand, a spoke structure of another mode ($\frac{2\pi}{3}$) is formed without magnetic priming. At the end, t=39.043 ns, the desired spoke structure is formed for both cases. In addition to spoke formation, they give a graph showing the instantaneous frequency change. That is shown in Figure 3.8. In that graph, the frequency of the desired π-mode is reached at 18.5 ns and stays at steady-state after that time with magnetic priming; however, without magnetic priming, that desired frequency is reached at 52.5 ns after oscillating between some other mode frequencies [31]. From those simulations given in [31] and [32], it can be concluded that the magnetic priming technique reduces the start-up time and eliminates the mode competition successfully.

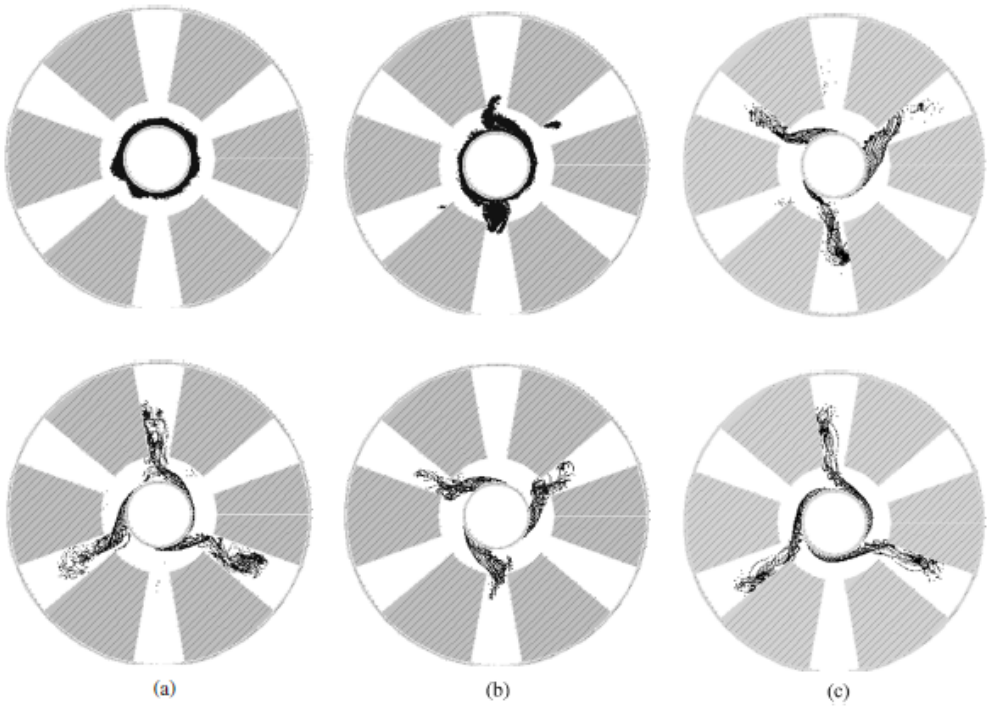

Figure 3.7: Comparison of electron spoke formation with (at bottom) and without (at top) magnetic priming : (a) t=13.536 ns, (b) t=17.345 ns and (c) t=39.043 ns [31]

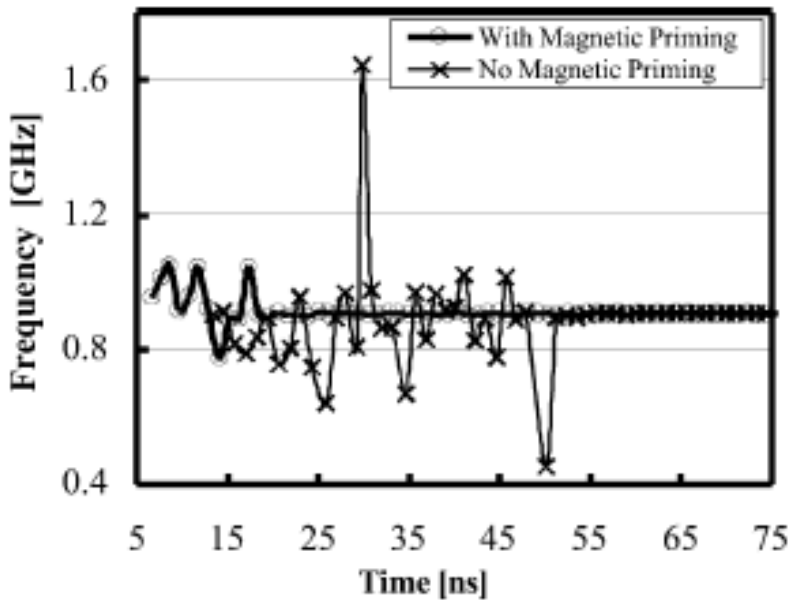

Figure 3.8: Comparison of the instantaneous output frequency with and without magnetic priming [31]

3.1.3 Electric Priming

The electric priming is another technique which provides the pre-bunching of the electrons in the A-K gap. In the technique, DC E-field is used in order to form periodic bunches of the electrons in a manner that supports the desired mode. E-field over the A-K gap is perturbed periodically in azimuth. To simplify the description of the process, a planar magnetron is taken into account first. That type of structure is given in Figure 3.9. In such a geometry, an electron at the origin point follows a trace as in Figure 3.10 under the influence of uniform E-field and B-field. If that E-field is perturbed periodically in y direction

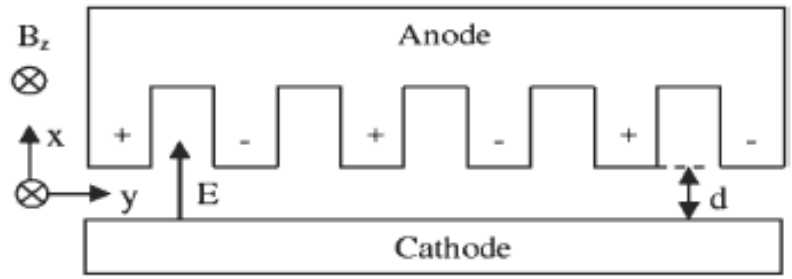

Figure 3.9: Planar magnetron structure [33]

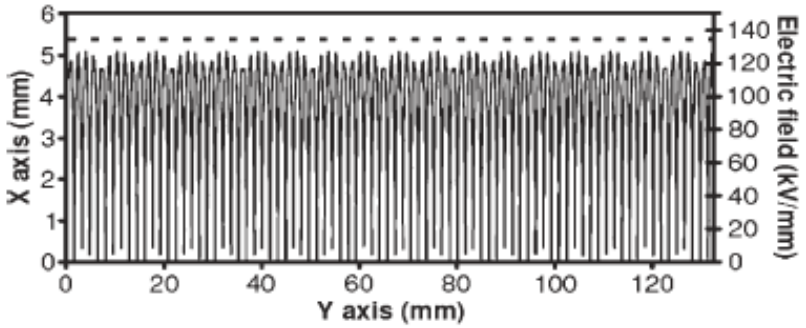

Figure 3.10: Trace of an electron under the uniform E-field in a planar magnetron structure [33]

according to Equation (3.2), the trace of the electron changes into periodically modulated one in the direction of y-axis [33]. That new trace can be seen in

Figure 3.11.

$$E = E_x\left[1 + \alpha sin(\frac{2\pi}{T}y)\right] \tag{3.2}$$

where E_x is the base electric field, α is the electric priming strength and T is the period.

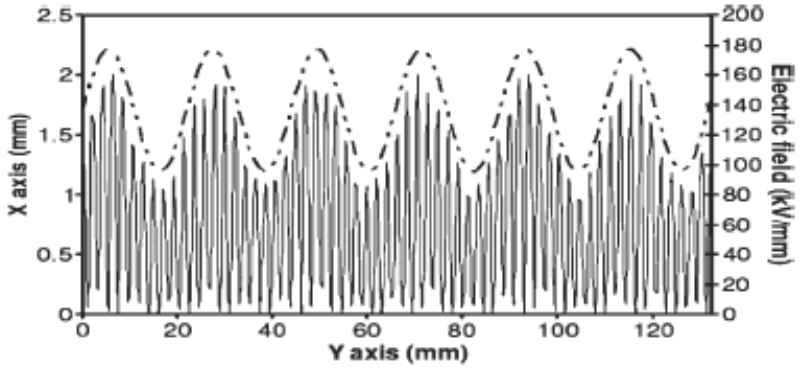

Figure 3.11: Trace of an electron under the perturbated E-field in a planar magnetron structure [33]

Maurya et al. realize the electric priming technique in a six-cavity magnetron by perturbing the E-field over the A-K gap through the insertion of protrusions and recessions on the anode vanes in an alternating manner. The structure they suggest is in Figure 3.12. That structure helps the formation of a six-fold spoke structure of the desired 2π-mode operation. In their paper, the simulation result of the output power and the output frequency spectrum are given as in Figure 3.13. From the output power results, it can be said that the structure consisting of alternating protrusions and recessions makes the start-up of faster because the output power reaches the steady-state value earlier with electric priming using alternating protrusions and recessions. The results of the output spectrum shows that the frequency spectrum component due to the mode competition does not exist with electric priming using alternating protrusions and recessions [33]. In another paper, they suggest a structure which has dielectric rods placed in the alternating cavities in order to perturb the E-field. The structure is given in Figure 3.14. The simulation results of that second structure is as in Figure 3.15 [34]. Those results also shows an improvement with the electric priming using the dielectric rods in the alternating cavities. However, the first structure seems more effective.

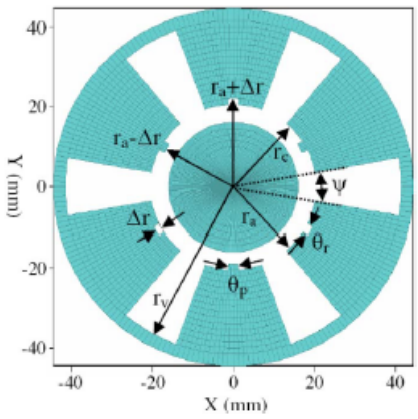

Figure 3.12: Magnetron structure with the electric priming using alternating protrusions and recessions [33]

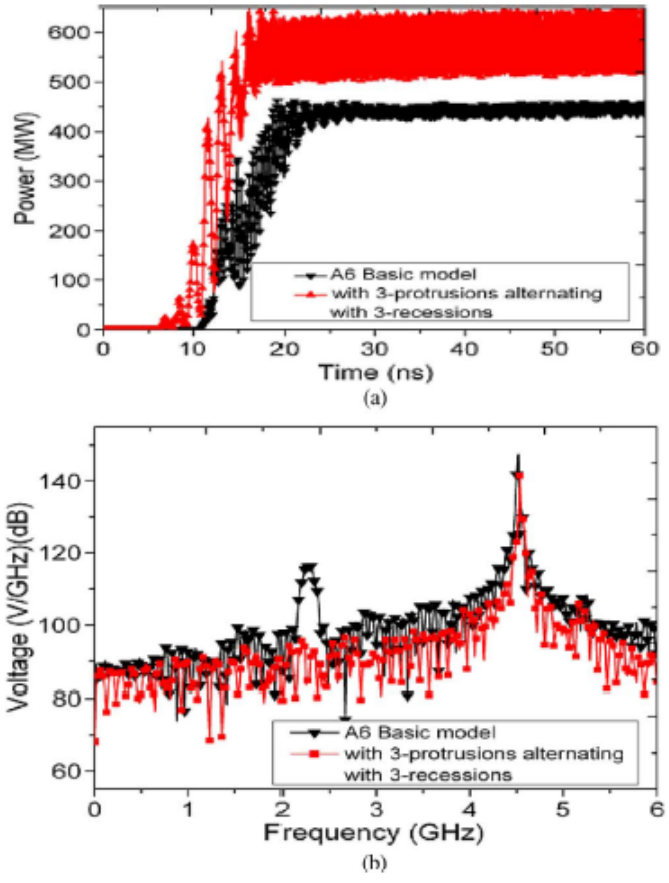

Figure 3.13: Comparison of the output power and the spectrum with and without the electric priming using alternating protrusins and recessions : (a) The output power and (b) The output spectrum [33]

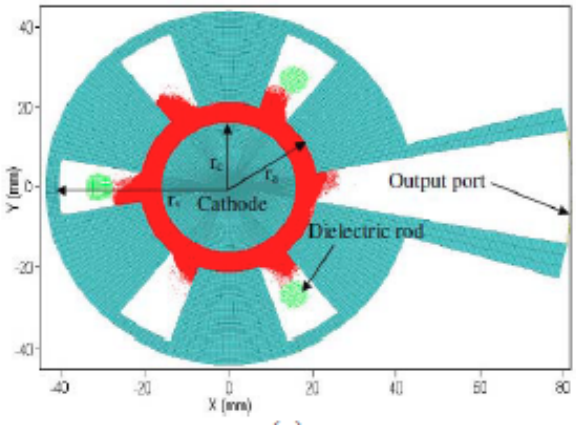

Figure 3.14: Magnetron structure with the electric priming using dielectric rods in alternating cavities [34]

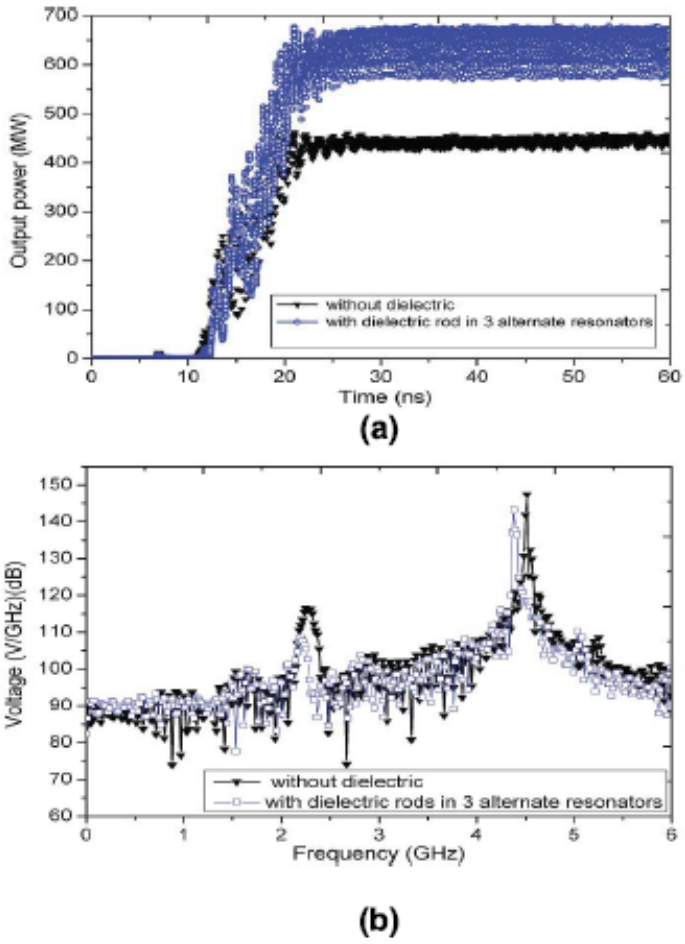

Figure 3.15: Comparison of the output power and the spectrum with and without the electric priming using dielectric rods in the alternating cavities : (a) The output power and (b) The output spectrum [34]

The studies on the electric priming in [33] and [34] provides an improvement in the start-up time of a magnetron and the elimination of the mode competition. Since the electric priming technique in those studies is obtained by alterations in anode structure, this technique can also be named as anode priming technique. However, the electric priming can also be obtained by changing the other structures in the magnetron such as the cathode.

3.1.4 RF Priming

Priming techniques described in previous sections aim to pre-bunch the electron cloud in the A-K gap and to speed up the start-up. However, in the RF priming technique, that is not the case. Instead, the RF priming technique is directly applied on the RF oscillations in the cavities of the magnetron. That technique is a basic type of the injection-locking in which different oscillators are locked in terms of the frequency and the phase. In the technique, a signal from a priming oscillator is injected into the cavities of the driven magnetron whose start-up time is intended to decrease [23]. Since the injected signal forces the oscillations in the cavities to the frequency of its own, the desired mode start-up is speeded up and the undesired modes are eliminated.
In their study, White et al. carry on experiments on the RF priming technique by using the test setup as in Figure 3.16. In the test setup, the signal from the priming source is injected into the main magnetron's cavity via a waveguide and the output signal is taken from another cavity. There are couplers to measure the input and the output powers, coils to measure the currents, and voltage monitors to measure the voltages. They carry on experiments for two cases. In one case Adler's relation in (3.3) is satisfied and in the other, it is not.

$$\frac{P_i}{P_o} \geq Q^2 \left(\frac{|\omega_i - \omega_o|}{\omega_o} \right)^2 \tag{3.3}$$

where P_i is the priming oscillator power, P_o is the driven oscillator power, Q is the quality factor, ω_i is the priming radian frequency and ω_o is the driven radian frequency. That relation is the condition for injection-locking of two signals and it means that if the power of the injection signal is sufficiently high or the difference between the frequencies of two signal is sufficiently small, then,

those two signals can be locked into together. The results of their experiment are given in Figure 3.17, in which the time delay before the start of the oscillations is shown, and in Table 3.1, in which the desired mode power, the undesired mode power, the time delay before the start of the oscillations and output pulse widths are supplied [23].

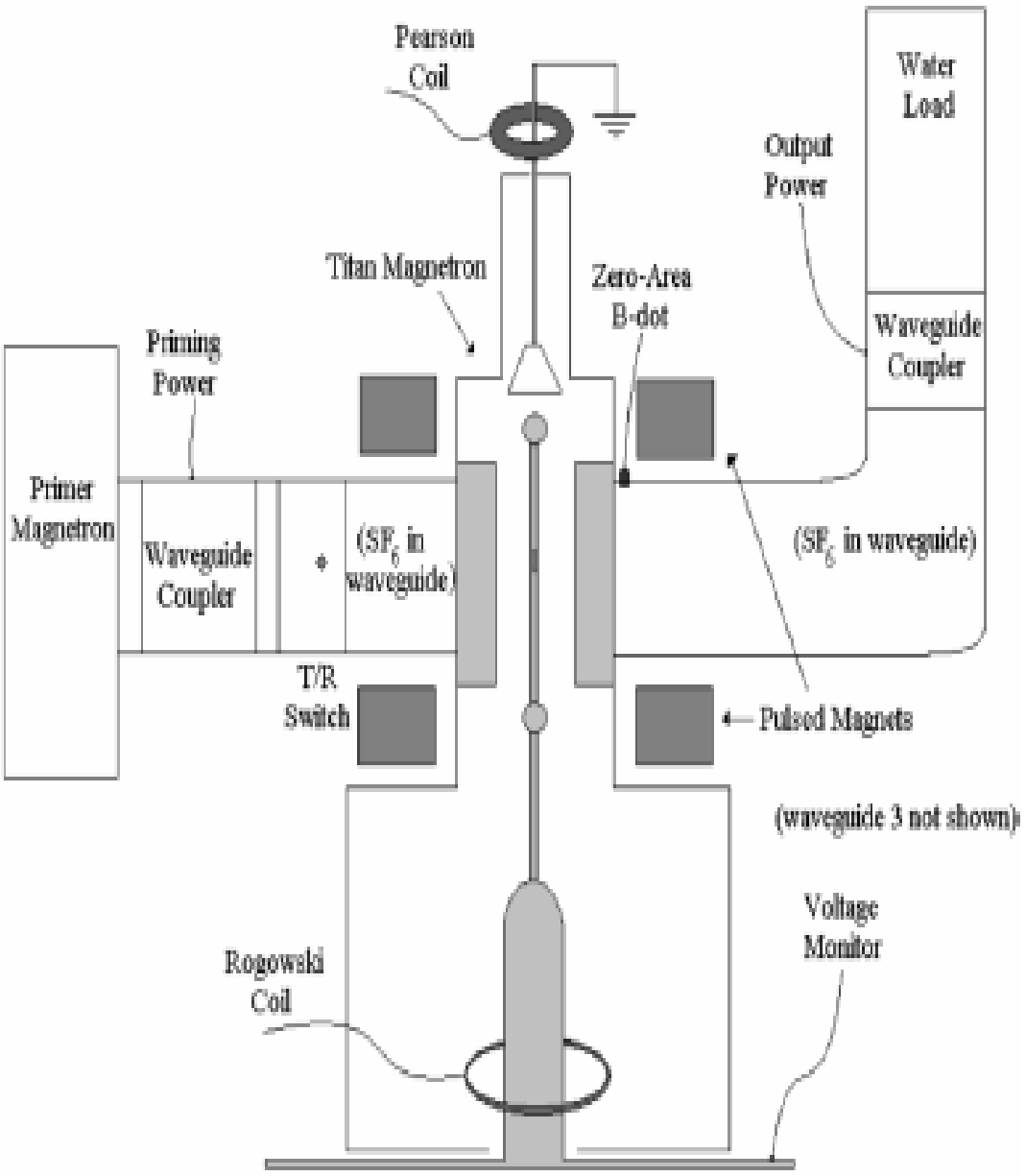

Figure 3.16: Test setup used in RF priming tests [23]

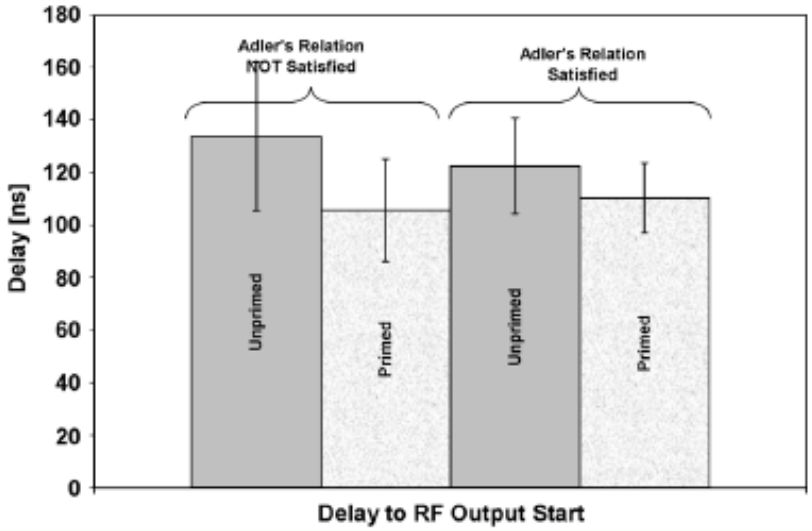

Figure 3.17: Comparison of the start-up time with and without the RF priming [23]

Table3.1: Comparison of the start time and the mode competition with and without the RF priming : Adler's relation satisfied (CASE I) and not satisfied (CASE II) [23]

PARAMETER	CASE I		CASE II	
	Unprimed	Primed	Unprimed	Primed
Desired Mode Power (MW)	5.9	5.7	0.9	1.1
Undesired Mode Power (MW)	7.5	4.4	0.8	0.4
Delay (ns)	134	105	123	110
Output Pulse Width (ns)	195	218	195	208

Observing the results in Figure 3.17, the time delay before the start of the oscillations is smaller for both cases of Adler's relation when RF priming is applied. In addition, the data in Table 3.1 shows smaller time delay before the start of the oscillations, less undesired mode power and longer pulse width for the case of the RF priming. Therefore, it can be said that the RF priming improves the start-up time and eliminates the mode competition. In addition, it can be concluded that locking of two signals is not necessary in order the RF priming to be useful because there are improvements for both cases of Adler's relation.

3.2 Transparent Cathode

At the beginning of the chapter, two factors effective in the start-up of a magnetron were defined as the start conditions and the rate of build-up [25]. In the previous sections, the priming techniques improving the start conditions were discussed. However, those priming techniques have nothing to do with the rate of build-up and it is yet to be improved. The structure which improves the rate of build-up in addition to provide three of the priming techniques is the transparent cathode [35]. The transparent cathode is a cathode type which has discrete longitudinal emitting strips formed by removing the material around a hollow cylinder [36]. The structure of the transparent cathode is given in Figure 3.18. The name transparent is due to the cathode's transparency to the TE modes of the magnetron operation [25].

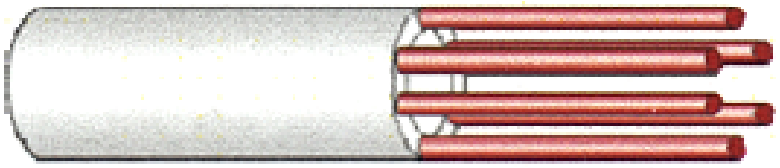

Figure 3.18: Transparent cathode structure [35]

The rate of build-up is the increment of the growth of the oscillations in the magnetron. That increment can be formulated as [37],

$$Im\omega \approx \frac{\omega}{4Q}\left(\sqrt{1+\chi_s \frac{eE_0}{mc^2}\left(\frac{4Qc}{\omega}\right)^2 \frac{S_c}{V}} - 1\right) \tag{3.4}$$

where ω is the radian frequency, Q is the quality factor, e is the electron charge, m is the electron mass, c is the speed of light, E_0 is the radial DC E-field, S_c is the cathode area and V is the total volume storing EM energy. χ_s is the ratio of the square of the azimuthal E-field on the electron cloud to the squared average E-field in the resonant system and it is as [37],

$$\chi_s = \frac{{E_\theta}^2(\Delta)}{\frac{1}{V}\int\limits_V |\vec{E}|^2 dV} \tag{3.5}$$

where $E_\theta(\Delta)$ is the azimuthal E-field on the electron cloud and V is the total volume storing EM energy. Equations (3.4) and (3.5) show that the rate of build-up depends on the strength of the synchronous azimuthal E-field, E_θ, on the electron cloud whose thickness is Δ. Strong E_θ on the cloud speeds up the energy transfer between the electrons and the EM fields in the cavities because it determines the radial velocity at which electrons get closer to the anode and it facilitates the electrons to be captured by the EM fields at the anode [37]. In radial direction, the synchronous azimuthal E-field is distributed as in Equation (3.6) for a standard solid cathode; on the other hand, that distribution is a modified Bessel function of the first kind of order n as in Equation (3.7) for a transparent cathode [25].

$$E_\theta(r) = E_\theta(r_a)\frac{sinh[g(r - r_c)]}{sinh(gd)} \tag{3.6}$$

$$E_\theta(r) = E_\theta(r_a)\frac{I_n(gr)}{I_n(gr_a)} \tag{3.7}$$

where r_a is the anode radius, r_c is the cathode radius, d is the A-K gap spacing $(r_a - r_c)$, g is the transverse wave number and n is the azimuthal index of the operating wave. Those distributions over the A-K gap for the solid and the transparent cathodes can be seen in Figure 3.19. In Figure 3.19, it is clear that

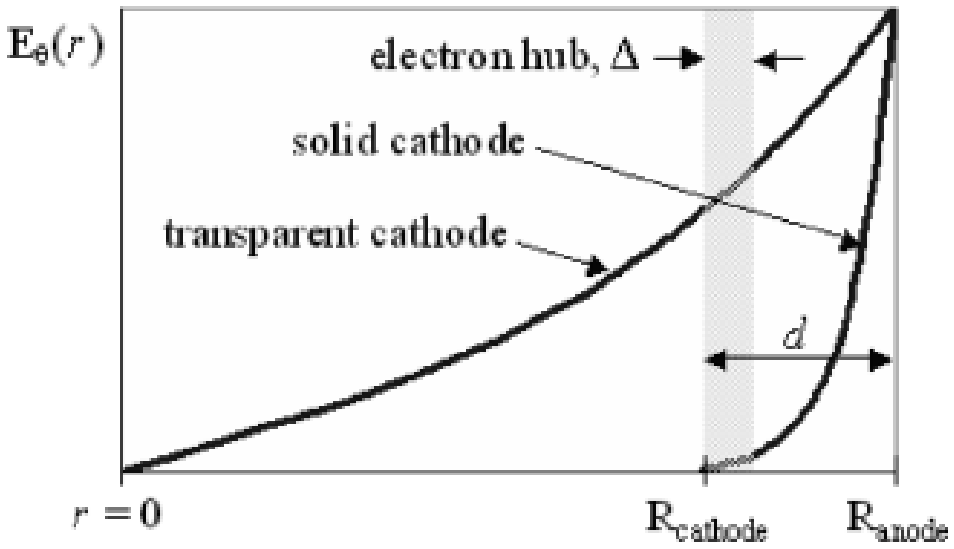

Figure 3.19: Synchronous azimuthal E-field distributions for the solid and the transparent cathodes [25]

the synchronous azimuthal field, E_θ, on the electron cloud is significantly higher for the transparent cathode than the solid one. That implies a faster start-up because of the higher rate of build-up.

In addition to the rate of build-up, the transparent cathode improves the start conditions owing to the priming techniques existing inherently. Those are the cathode priming, the magnetic priming and the electric priming. Because of the discreteness of the emitting strips on the cathode, the transparent cathode exhibits cathode priming [36]. Figure 3.20 shows the electron distributions in the A-K gap of the solid and the transparent cathode magnetrons at the start of the magnetron operation. With the transparent cathode, the bunches of the

(a) Transparent (b) Solid

Figure 3.20: Distribution of the electrons in the A-K gap at the start of the magnetron operation with the solid and the transparent cathodes [36]

electrons are formed at the start while there exists a uniform electron cloud with the solid one. Since there are six strips in the transparent cathode, the formed bunches support the desired 2π-mode operation of that six cavity magnetron.

The magnetic priming is exhibited by the transparent cathode due to the axial currents, shown in Figure 3.21,along the longitudinal strips which produces axially variable azimuthal B-fields around the strips according to Ampere's law [36]. Those axially variable azimuthal B-fields cause the formation of azimuthally variable axial B-fields in the interaction region because of Maxwell's equation of $\vec{\nabla} \times \vec{H} = 0$. Those azimuthally variable axial B-fields modulates the electron cloud azimuthally as desired and that is the magnetic priming in the transparent cathode [25].

The last priming technique exists in transparent cathode is the electrical prim-

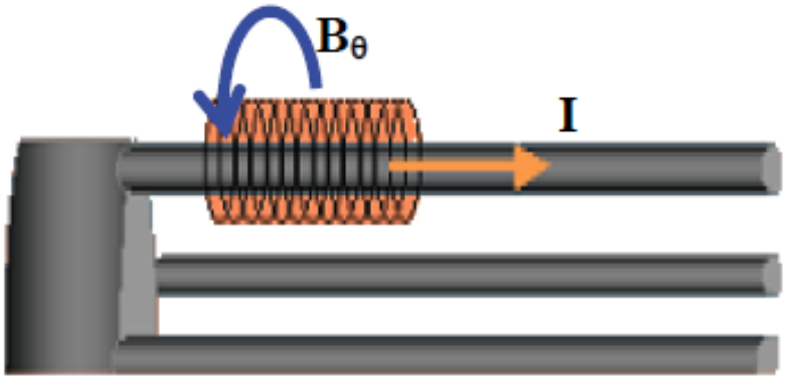

Figure 3.21: Magnetic field formation around the strips of the transparent cathode [36]

ing. It is formed due to the fact that the discrete structure of the strips causes non-uniform electron cloud thickness around the cathode and that modulates the radial E-field azimuthally. That modulated E-field implies the electrical priming [36].

In their paper Bosman et al. simulate the transparent cathode magnetron and compare it with a standard solid cathode and a solid cathode with cathode priming. The power and current graphs of that simulation with respect to time are as in Figure 3.22. Those graphs show the improvement of the transparent cathode such that the output power and the anode current in the graphs reach steady-state at 40 ns for the solid cathode, at 15.5 ns for the solid cathode with the cathode priming and at 14 ns for the transparent cathode [25].

Prasad et al. carry experiments on the transparent cathode in their paper. The output power results is given in Figure 3.23. The results show the faster start-up in the transparent cathode [36].

In conclusion, the transparent cathode helps faster start-up time by improving the start conditions owing to inherently existing priming techniques and increasing the rate of build-up due to the strong synchronous azimuthal E-field on the electron cloud.

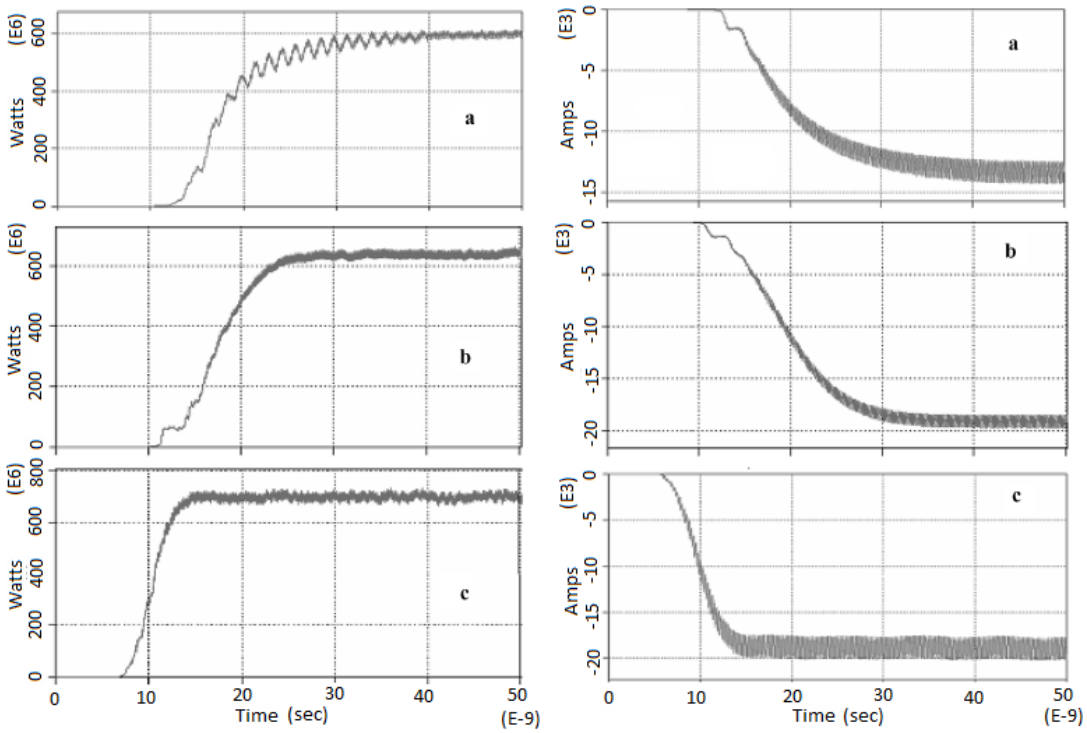

Figure 3.22: Comparison of the output power (left) and the anode current (right) with the solid cathode (a), the solid cathode with the cathode priming (b) and the transparent cathode (c) in a simulation [25]

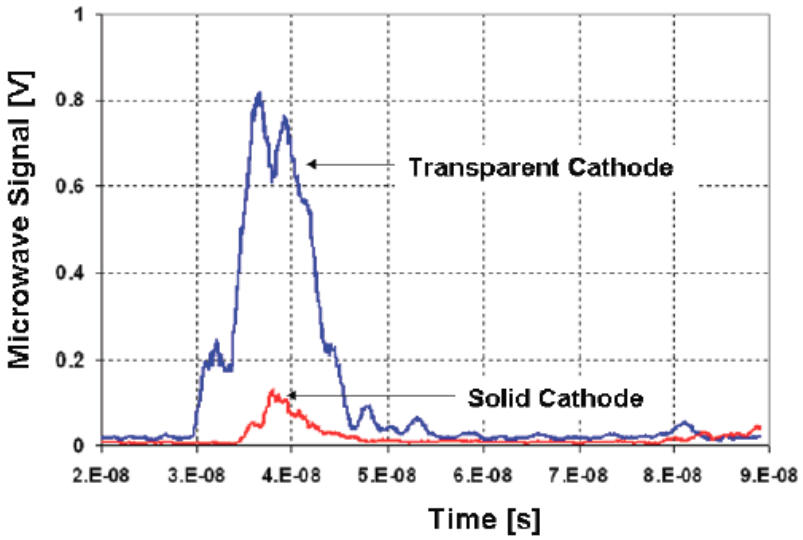

Figure 3.23: Comparison of the output power with the solid cathode and the transparent cathode in an experiment [36]

CHAPTER 4

SIMULATIONS ON FAST START-UP TECHNIQUES IN MAGNETRONS

4.1 Simulation Environment

The simulation environment used in the thesis in order to observe the operation and the parameters of the magnetron is MAGIC. It is a software composed of some tools that allow users to arrange the geometry, the material properties, the boundary conditions, the field algorithms, the particle algorithms and the output specifications of an EM problem consisting of particles [38]. A schema which shows the process of the software in one cycle is given in Figure 4.1.

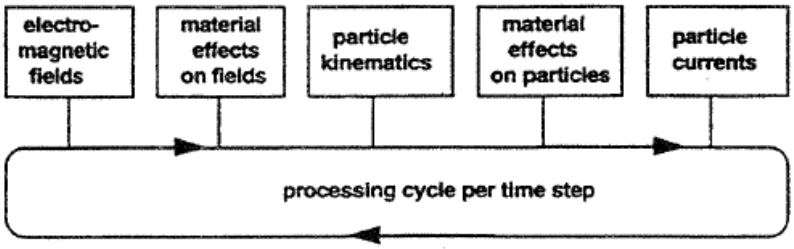

Figure 4.1: The schema showing the processing cycle of MAGIC [38]

MAGIC solves the plasma physics processes in which there exists interactions between EM fields and space charge by using FDTD (Finite Difference Time Domain) method in the PIC (Particle-in-Cell) basis. In that approach, starting from a specified initial conditions, time domain Maxwell's equations are used together with Lorentz force equation and the continuity equation in order to get the solution of the EM fields and to determine the traces of the particles under those fields over time [39]. MAGIC uses Maxwell's Equations (4.1) and particle

kinematics in Equations (4.2) [38],

$$\partial_t \vec{B} = -\vec{\nabla} \times \vec{E}, \qquad \partial_t \vec{E} = -\frac{\vec{J}}{\varepsilon} + \frac{\vec{\nabla} \times \vec{B}}{\mu\varepsilon}, \qquad \vec{\nabla} \cdot \vec{E} = \frac{\rho}{\varepsilon}, \qquad \vec{\nabla} \cdot \vec{B} = 0 \quad (4.1)$$

$$\vec{F_i} = q_i\big[\vec{E}(\vec{x_i}) + \vec{v_i} \times \vec{B}(\vec{x_i})\big] = m_i \partial_t \vec{p_i}, \qquad \partial_t \vec{x_i} = \vec{v_i}, \qquad \vec{v_i} = \frac{\vec{p_i}}{\gamma_i} \qquad (4.2)$$

where $\vec{E}$ is the E-field, $\vec{B}$ is the B-field, $\vec{J}$ is the current density, ρ is the charge density, ε is the permittivity of the simulation space, μ is the permeability of the simulation space, $\vec{F_i}$ is the force on the ith particle, $\vec{x_i}$ is the position of the ith particle, $\vec{v_i}$ is the velocity of the ith particle, $\vec{p_i}$ is the momentum of the ith particle, q_i is the charge of ith particle, m_i is the mass of the ith particle and γ_i is Lorentz factor. Since the FDTD algorithm is used, the integration is found by calculating the ratio between the difference of the new and the old variable values and the fixed time interval. The time grid used in the algorithm can be seen in Figure 4.2. The simulation space is divided into grids. One cell of the spatial grid and the field definitions on that cell is as in Figure 4.3.

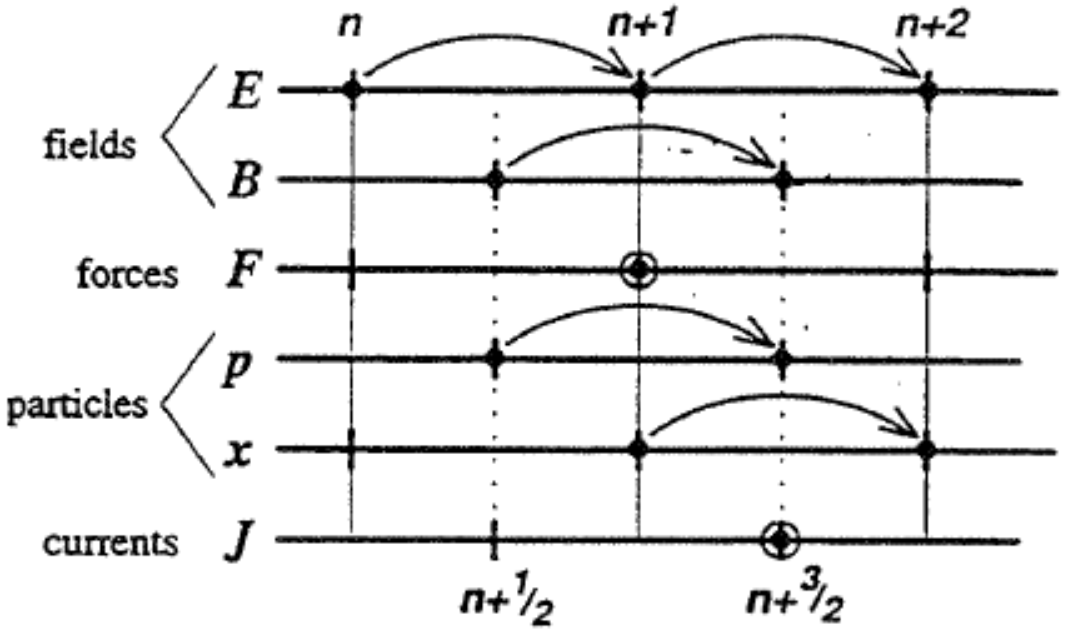

Figure 4.2: Time grid used in MAGIC FDTD algorithm [38]

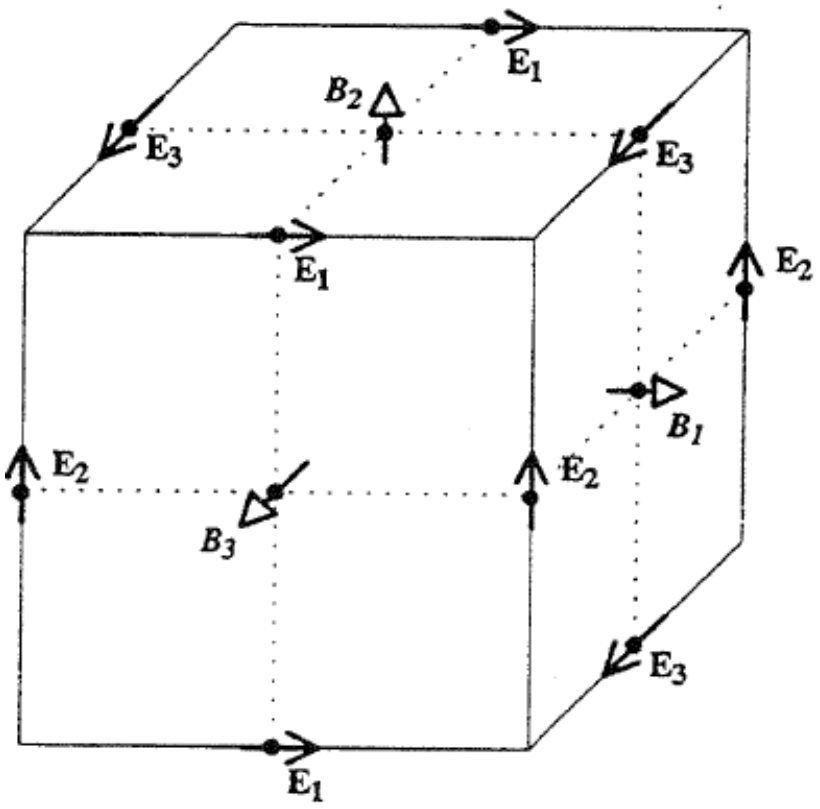

Figure 4.3: One spatial cell used in MAGIC FDTD algorithm and the field definitons on it [38]

4.2 A6 Magnetron

The magnetron chosen for the simulations throughout the thesis is A6 magnetron. It is a six-cavity relativistic magnetron. The reason behind the choice of A6 magnetron is that it is a mature one and most of the studies on the area have been carried out with that magnetron [25]. The cross-section of the basic A6 magnetron structure is given in Figure 4.4 and the dimensions are given in Table 4.1. In those figure and table, r_c is the cathode radius; r_a is the anode radius; r_v is the external radius of the vanes; ψ is the angular width of a cavity; N is the number of the cavities; and L is the axial length of the cavities.
Palevsky and Bekefi give a plot showing the voltage and axial B-field values at which A6 magnetron operates in their report in which they explain the design criteria of A6 magnetron [40]. It can be seen in Figure 4.5. In the figure, the

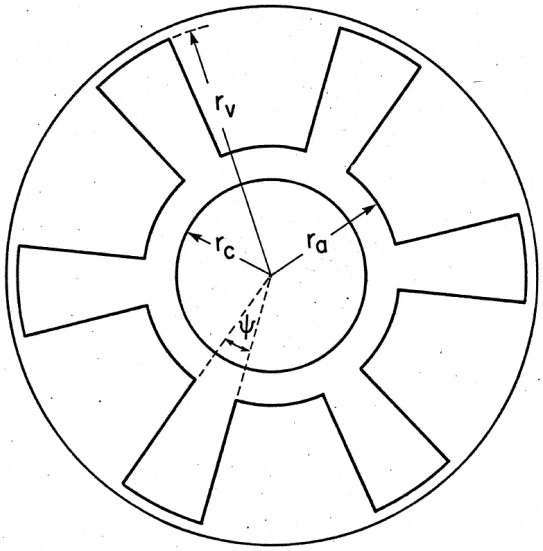

Figure 4.4: Cross-section of A6 magnetron structure [40]

Table4.1: Dimensions of A6 magnetron [40]

r_c (cm)	r_a (cm)	r_v (cm)	ψ (degrees)	N	L (cm)
1.58	2.11	4.11	20	6	7.2

dashed line corresponds to the operation range of the A6 magnetron. They also provide a dispersion diagram showing the frequency of the modes of A6 magnetron as in Figure 4.6. In that diagram, the frequency of the 2π-mode operation, which is the investigated mode throughout the thesis, is 4.60 GHz.

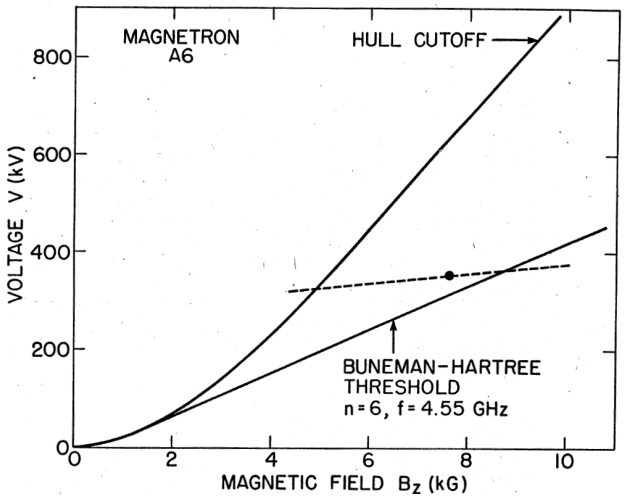

Figure 4.5: Operation range of A6 magnetron [40]

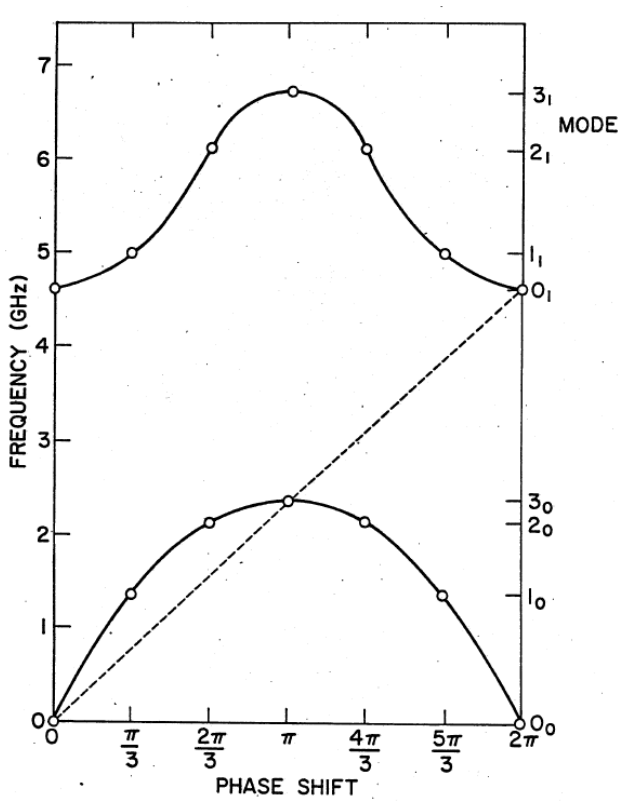

Figure 4.6: Dispersion diagram of A6 magnetron [40]

4.3 Simulation Model

4.3.1 Geometry

The purpose of the simulations was to compare a standard solid cathode magnetron, a solid cathode magnetron with cathode priming and a transparent cathode magnetron. A6 magnetron was chosen as the basis for all three type of technique. The first thing done was forming a model for the basic A6 magnetron. The model consists of three main blocks which are the cathode, the anode block and the backwall. Those blocks are given in Figure 4.7.

In Figure 4.7, (a) is the cathode structure that is a solid cylinder with the radius of 1.58 cm and the axial length of 10.8 cm. (b) is the anode block that is a hollow cylinder with the inner radius of 2.11 cm, the outer radius of 4.11 cm and the axial length of 7.2 cm. That anode block carries six cavities on it and it is closed

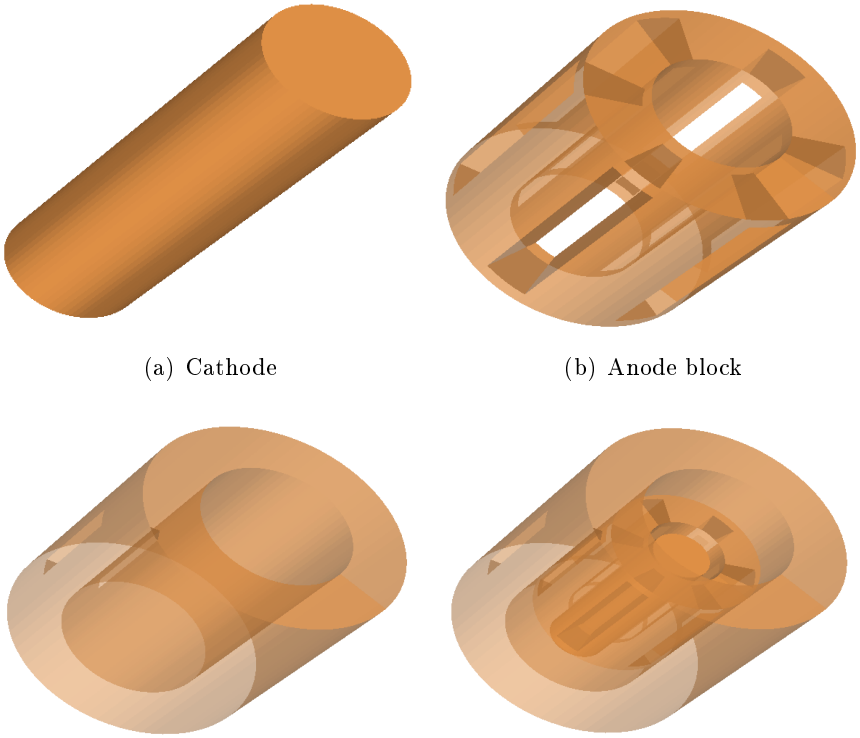

(a) Cathode (b) Anode block

(c) Back wall (d) A6 magnetron model

Figure 4.7: Model of the basic A6 magnetron

with the metal caps at both ends. (c) is the back wall structure that is also a hollow cylinder with the inner radius of 4.11 cm, the outer raius of 7.11 cm and the axial length of 14.4 cm. The back wall has a slot on it in order RF output to be coupled to a waveguide (WG). Those three are combined in a concentric manner to form the basic A6 magnetron model at (d). The arrangement can be seen more clearly on the cross-sectional views given in Figure 4.8. In the figure, (a) is the cross-section in r-φ plane. At the center, there is the cathode structure that has 1.58 cm radius. It is surrounded by the anode structure with the inner radius of 2.11 cm and the region between them is the interaction region, or A-K gap. The anode structure has six cavities and each of them has the angular width of 20°. The radial width of the cavities is 2 cm. Each cavity is separated by a vane structure that has angular width of 40°. The anode block surrounded by the back wall whose inner radius is 4.11 cm and radial width is 3 cm. At the end of the one cavity, there is a WG slot through the back wall and its angular width is 10°. (b) is the cross-section in r-z plane. The cathode structure has two

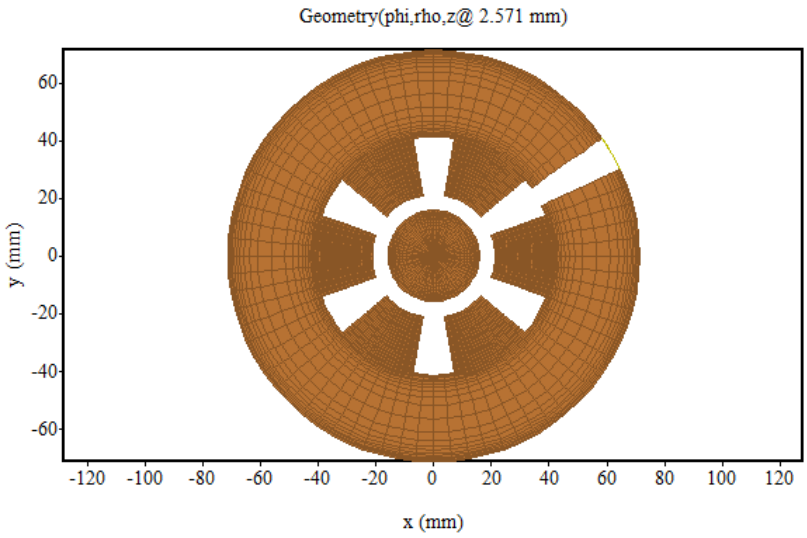

(a) Cross-section in r-φ plane

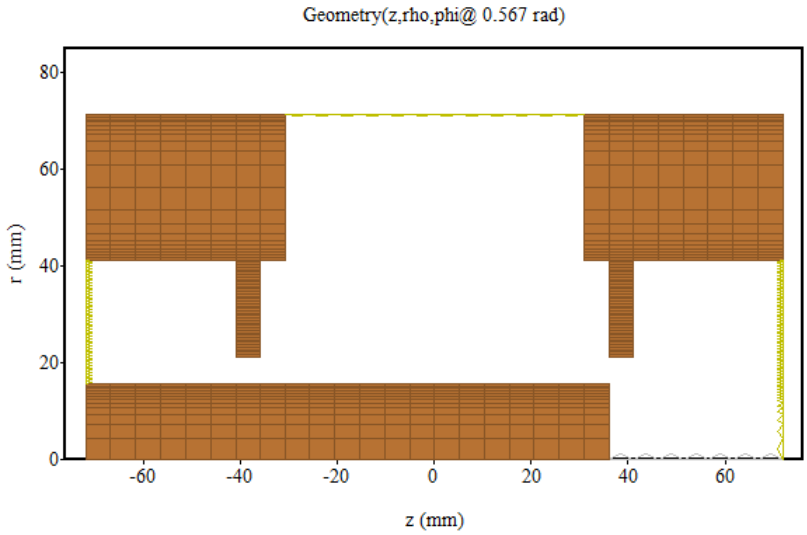

(b) Cross-section in r-z plane

Figure 4.8: Cross-sectional view of the basic A6 magnetron model

portion. One is the stem portion at the left which is placed in order the input DC voltage to be applied to the port region between the cathode and the back wall at the left of the figure. The axial length of the stem portion is 3.6 cm and there is no electron emission on that portion. The other one is the core portion whose axial length is 7.2 cm and that portion is the emitting one. Across the core portion of the cathode, there is the one of the six cavities that have the axial length of 7.2 cm. At the both end of the cavity, it is closed by the end

caps having the axial length of 5 mm. The cavity is the one in which the output power is extracted. Therefore, the coupling WG slot, which have 6.2 cm axial length, exists at the outer radius of the cavity.

The simulation grid structure of the basic A6 magnetron model can be seen in Figure 4.8. The cell sizes along the azimuthal (φ) direction and the axial (z) direction are arranged as uniform. Those are 5° in azimuth and 5 mm in axial direction. The radial cell size changes depending on the radial position. Starting from the center of the cathode, which is the origin of the simulation grid, to the 2 mm inner of the outer surface of the cathode, eight cells are placed along the radial direction in a manner that the sizes of the cells along the radial direction monotonically decrease and the last cell at the 2 mm inner of the cathode surface has 0.5 mm radial size. Between the 2 mm inner of the cathode surface and the 1 mm outer of the cavities, the uniform cell size of 0.5 mm is used. After that region, to the 1 mm inner of the outer surface of the back wall, sixteen cells are placed radially. The eight of them have size that monotonically increase starting with 0.5 mm radial size at the 1 mm outer of the cavities to the middle of the region consisting of those sixteen cells. The other eight of them are placed starting that middle position and have monotonically decreasing size ending with 0.5 mm radial size at the 1 mm inner of the outer back wall surface. From that position to the outer surface of the back wall, the radial cell size is arranged as 0.5 mm uniformly. That sizing of the cell in the radial direction is because of the trade-off between the accuracy of the results and the simulation time. If a uniform 0.5 mm cell size was chosen in the radial direction, the simulation time would be excessive and the memory would be insufficient. However, the fine resolution is required in the A-K gap in which the electrons exist and in the cavities. Therefore, that non-uniform cell size along the radial direction was chosen.

In the model, there are three ports being the outer boundary for the simulation and they allow the outgoing and incoming waves according to defined conditions. Those ports close the model and separate the interior of the simulation, which is vacuum, from the external world. They are shown in Figure 4.9. In the figure, black shaded areas represent the ports. The input port is the one at which input voltage of the magnetron applied between the cathode and the

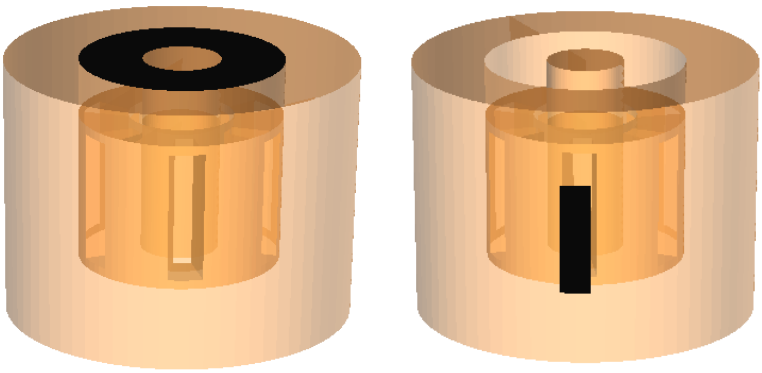

(a) Input port

(b) Output port

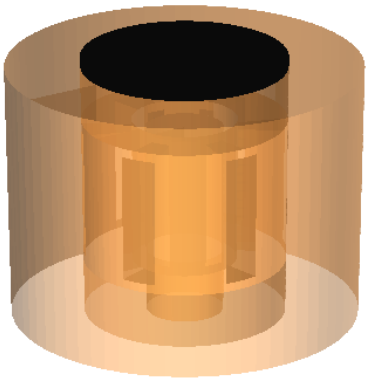

(c) Passive port

Figure 4.9: Ports defined in the basic A6 magnetron model

back wall. The RF output is extracted through the output port. The passive port is just absorbing wave port boundary and it is defined in order to enclose the simulation environment.

The basic A6 magnetron has a solid cathode and the emission occurs on the entire surface of that cathode structure to the interaction region. The emission regions on the cathode surface in the model are defined as in Figure 4.10. The blue areas are the emitting regions on the cathode surface and simulation program emits electrons into those regions.

After the model for the basic A6 magnetron was formed, it was modified in order to obtain a model for A6 magnetron with the cathode priming. The model for the A6 magnetron with the cathode priming is the same with the basic A6 magnetron model except one aspect. The emission regions in that new model with cathode priming are discrete instead of being the entire surface. Those regions

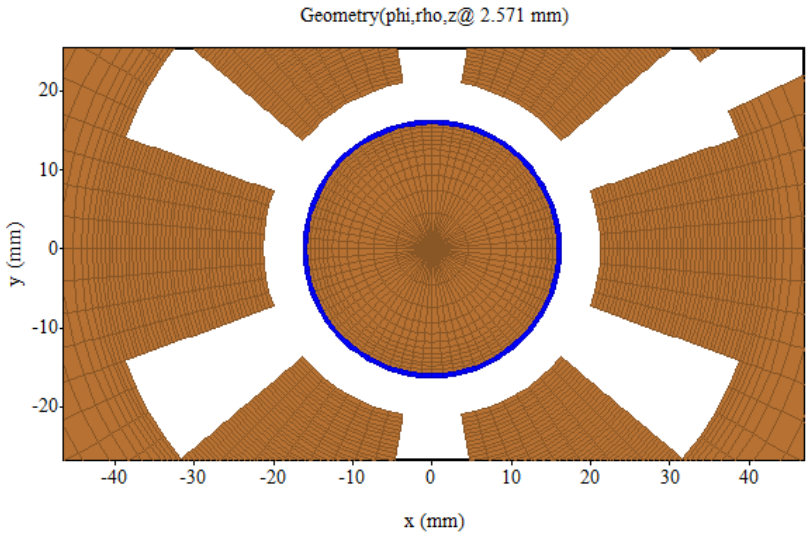

(a) r-φ plane

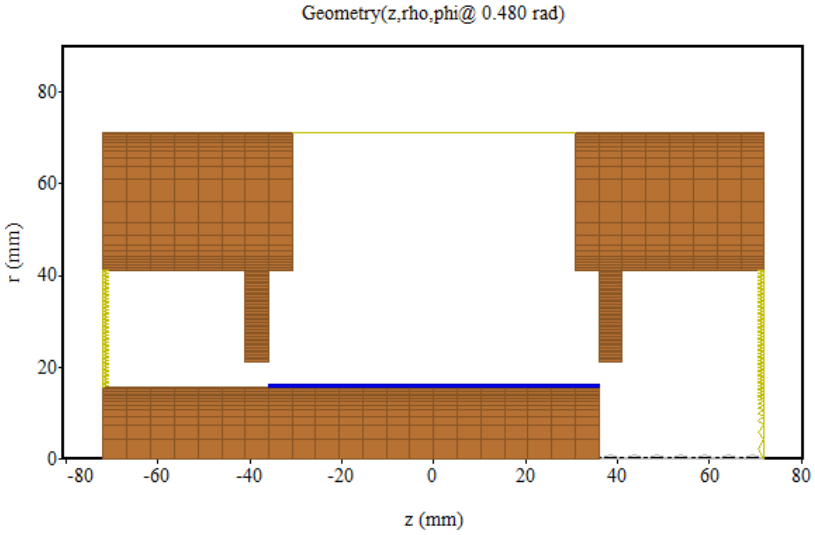

(b) r-z plane

Figure 4.10: Emission regions in the basic A6 magnetron model

can be seen in Figure 4.11. Blue areas are the emitting regions. There are six of those discrete emitting regions and they are arranged in such a way that the regions are across the vanes of the anode block and they have the angular width of 30°. In Figure 4.12, there are 3D views showing the emitting regions (blue areas) on the cathodes of the basic A6 magnetron model and the model of A6 magnetron with the cathode priming.

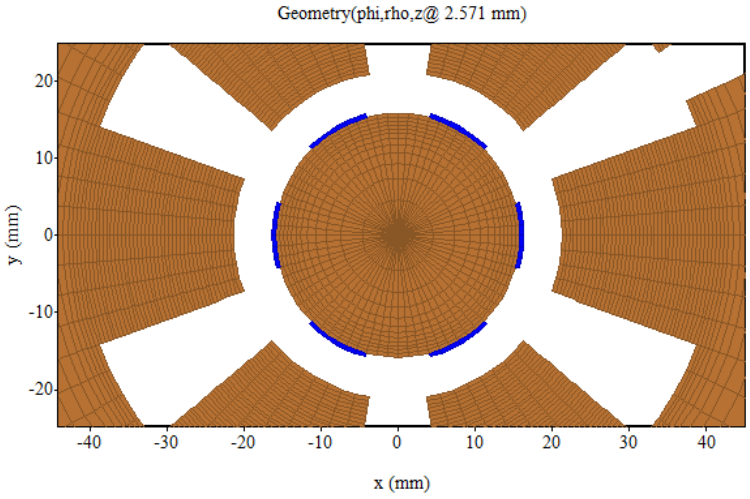

(a) r-φ plane

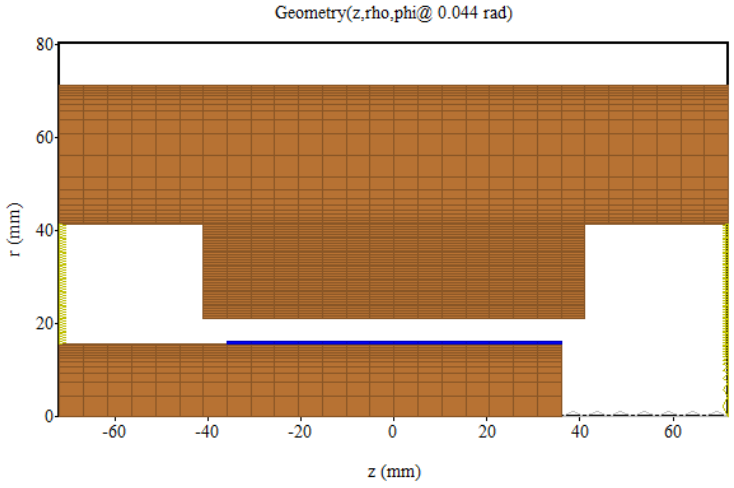

(b) r-z plane

Figure 4.11: Emission regions in the A6 magnetron with the cathode priming model

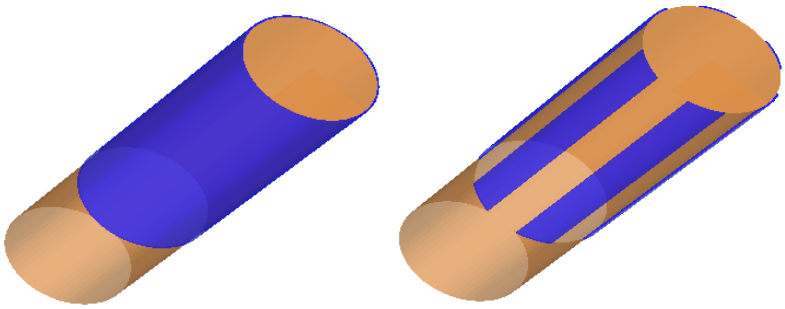

(a) Basic solid cathode (b) Cathode with priming

Figure 4.12: Comparison of emission regions of the basic A6 magnetron model and A6 magnetron with the cathode priming model in 3D view

The last model was formed for A6 magnetron with the transparent cathode structure. That model with transparent cathode differs from the basic A6 magnetron model with the solid cathode in two aspects and the rest parts of the models are the same. The first difference is the cell size of the grid in the azimuthal direction. In the transparent cathode magnetron model, the azimuthal cell size is 2.5° instead of the 5°. Otherwise, the accuracy of the results would not be sufficient because of the thin longitudinal strips on the cathode structure. The second difference is the model of the cathode structure. That cathode structure has discrete longitudinal strips arranged circularly and the interior of it is hollow. The 3D model of the transparent cathode structure is given in Figure 4.13. The cross-sectional view of the model of the A6 magnetron with

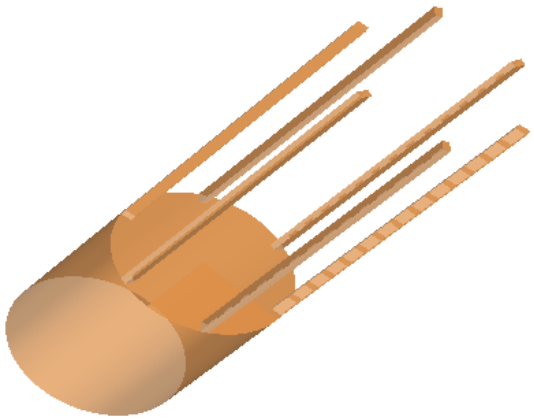

Figure 4.13: 3D model of the transparent cathode

the transparent cathode can be seen in Figure 4.14. The radial width of the cathode strips is 2 mm and they have angular width of 5°. The axial length is 7.2 mm as in the solid cathode. Those strips placed in an azimuthally periodic way and the outer radius of the circle that they form is the same as the solid cathode radius which is 1.58 cm. The position of the strips relative to the vanes is arranged such that the angle between the start of the vane and the start of the strip is $\theta = 10°$ as in (a) of Figure 4.14.

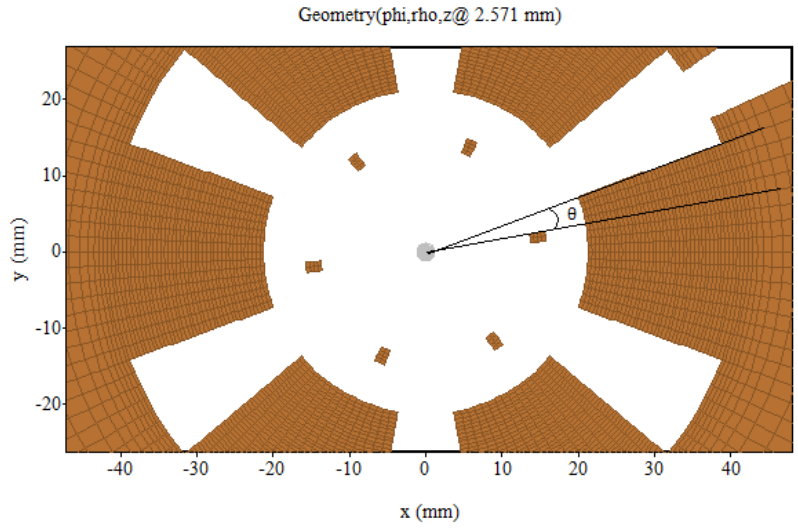

(a) Cross-section in r-φ plane

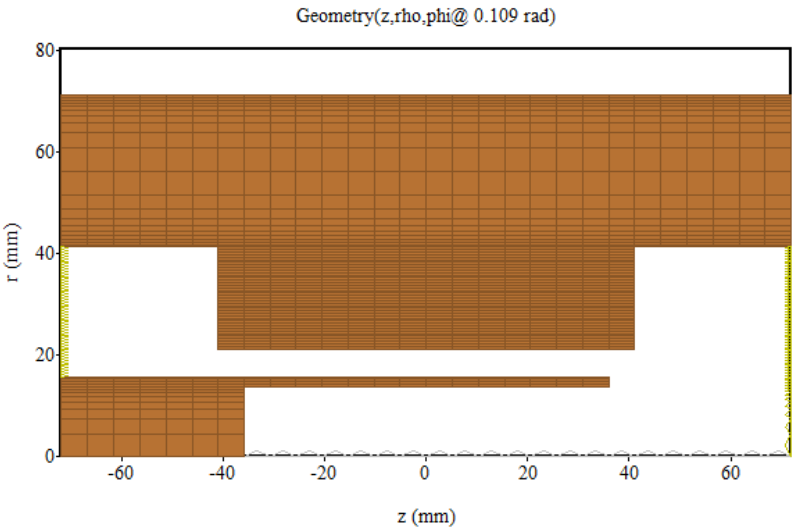

(b) Cross-section in r-z plane

Figure 4.14: Cross-sectional view of the A6 magnetron with the transparent cathode model

4.3.2 Input Parameters

There are two input parameters which were modeled. Those are the axial B-field and the voltage between the cathode and the anode. In the real case, the first one is supplied by the permanent magnets or the coils and those means provide a constant B-field over the interaction space. In the model, that axial B-field is applied by presetting a static B-field value in the axial direction over the

entire simulation space uniformly. The applied static and uniform B-field value is 0.52 T. The model of the second one is a voltage waveform which starts from zero at the beginning and reaches the desired radial voltage of the magnetron operation after a ramp type rise with a rise time. The desired radial voltage for the simulations is 350 kV and the voltage rise time is 10 ns. The function showing that waveform is,

$$VOLTAGE(t) = V_{radial} RAMP\Big(\frac{t}{t_{rise}}\Big) \tag{4.3}$$

where,

$$RAMP(x) = Max(0, Min(1, x)) \tag{4.4}$$

In the simulation environment, that voltage waveform is applied by setting the incoming wave (E-field) on the input port boundary in (a) of Figure 4.9. That incoming wave is set by defining a temporal function and a spatial profile function for the field vectors in the direction transverse to the propagation of the incoming wave. In this case, the propagation is along the axial (z) direction so the defined spatial profile vectors are along the radial (r) and the azimuthal (φ) directions. The defined temporal function is as in Equation (4.5) and the defined spatial profile functions for the field vectors along the radial and the azimuthal directions are as in Equation (4.6) and Equation (4.7), respectively.

$$DRIVER(t) = 0.7 V_{radial} RAMP\Big(\frac{t}{t_{rise}}\Big) \tag{4.5}$$

$$E_r = \frac{1}{r} \tag{4.6}$$

$$E_\varphi = 0 \tag{4.7}$$

The spatial function in Equation (4.6), which is along radial direction, is normalized over a line from cathode to anode such that its integral of E-field over that line is unity in order to make the unit of the temporal function in Equation (4.5) to be volts. Since the defined wave is the incoming one, a command in the simulation environment, which rescales that incoming wave according to the observed input voltage value in the simulation, is used in order to arrange the total field, which is the addition of the incoming and the reflected waves, and obtain the desired voltage waveform in Equation (4.3) at the port boundary.

That command uses rescaling function [39],

$$rescale(t) = exp\left[\frac{1}{\delta t}\left(1 - \frac{\delta t}{t}\right)\int_0^t \left(1 - \frac{observed(t')}{desired(t')}\right)dt'\right] \tag{4.8}$$

where δt is the time constant. After observation on the input voltage waveforms in the simulations, the time constant, δt, in equation (4.8) was determined as T/8, where T = 218.34 ps is the period of the output RF signal at frequency 4.58 GHz (2π-mode operation frequency of the A6 magnetron). For some different values of the time constant, observed input voltages on the port can be seen in Figure 4.15. In that figure, it is obvious that the higher the time constant, the

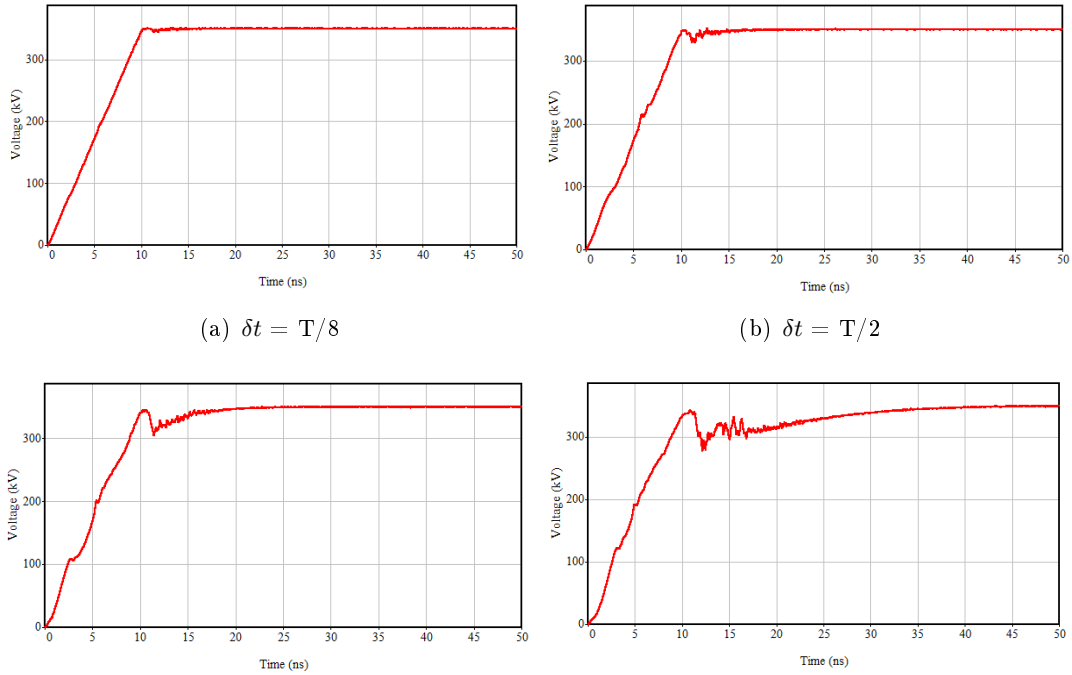

(a) δt = T/8 (b) δt = T/2

(c) δt = 2T (d) δt = 8T

Figure 4.15: Input voltages in the simulations for the different time constants

worse the input voltage waveform. On the other hand, the time constant cannot be very small; otherwise, the simulation fails due to the instability. As a result of that information, T/8 value was chosen as the time constant. The input voltage waveform which was applied in the simulations is as in Figure 4.16.

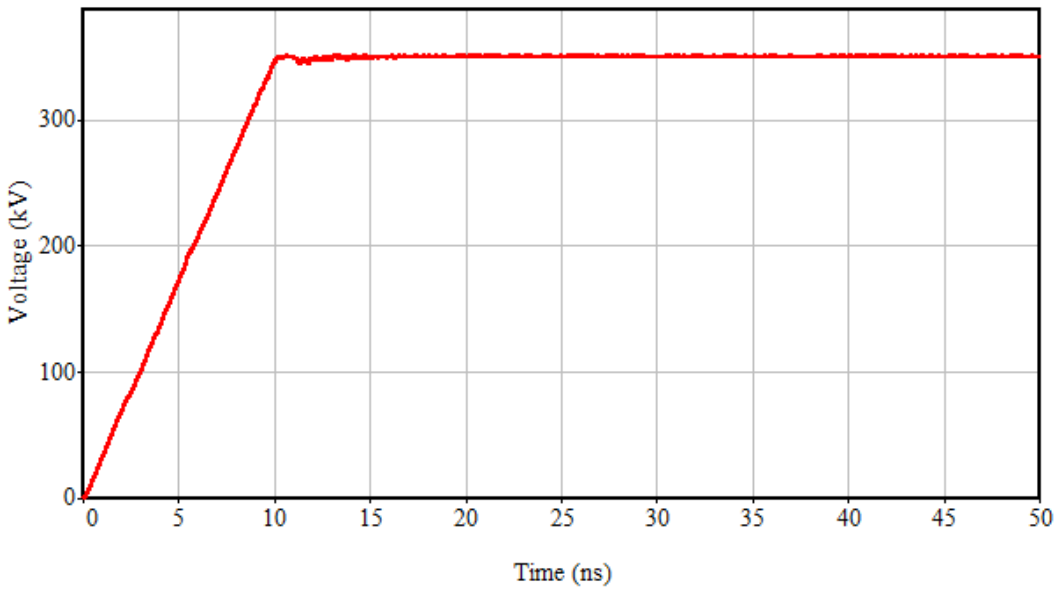

Figure 4.16: Input voltage waveform used in the simulations

4.3.3 Emission

For the emission process in the simulations, the default explosive emission model of the simulation environment was used. In that model, threshold E-field, which is the field value such that the cell on the emitting surface breaks down and starts to emit particles when that value is exceeded by the E-field at that cell, is 2.3×10^7 V/m. In the model, the emission occurs on the emitting surface according to formula [39],

$$\frac{dq}{dA} = \varepsilon_0 f(t - t_b)(E_c - E_r) - \rho \tag{4.9}$$

where $f(t)$ is the plasma formation rate, t_b is the time at which the cell breaks down, E_c is E-field at the cell, E_r is the residual field at the surface and ρ is the existing charge density at the surface. In the used default model, residual E-field, E_r, is 0 V/m and the plasma formation rate is linear with a 5 ns rise time, τ, as [39],

$$f(t) = \begin{cases} \frac{t}{\tau} & \text{if } t < \tau \\ 1 & \text{if } t > \tau \end{cases} \tag{4.10}$$

4.4 Simulation Results

The simulations were carried out by applying the 0.52 T axial B-field and the voltage waveform in Figure 4.16 as the input parameters. The simulation runtime was chosen as 50 ns. Over that runtime some of the output parameters of the magnetron were observed. Those include the operating frequency and its evolution in time, the voltage oscillations in the output port, the output power and the current collected by the anode. In addition, the RF fields in the cavities and the particles in the A-K gap were investigated. From all those data, the speed of the start-up for the solid cathode A6 magnetron, the solid cathode A6 magnetron with the cathode priming and the transparent cathode A6 magnetron tried to be interpreted.

The first observation is the operating frequency. The output spectrums for the three types of magnetrons are given in Figure 4.17. The observed frequency for the solid cathode and the solid cathode with the cathode priming is 4.58 GHz, which is consistent with the theoretical value for A6 magnetron that is 4.60 GHz. On the other hand, the output frequency of the transparent cathode magnetron is 4.00 GHz. It can be said that the modification on the cathode shifted the output frequency. Apart from that, the output spectrum of the transparent cathode magnetron is more clear than the others. That shows the effect of the tranparent cathode structure on the mode competition and the noise.

The second observation is the evolution of the frequency over time. The time-frequency spectrogram graphs obtained from the simulation for the three types of the magnetrons are as in Figure 4.18. In the graphs, the solid cathode and the solid cathode with the cathode priming magnetrons first develop another frequency and then, reaches the operating frequency of the magnetron. The cathode priming structure reaches that frequency a little bit earlier than the solid one. However, the transparent cathode structure starts directly with the operating frequency and that start of the oscillations apparently earlier than the other structures. Those graphs show the faster start-up and the improved mode competition of the transparent cathode magnetron.

The voltage oscillations at the output slot as the third observation can be seen in Figure 4.19. The oscillations start around 9.5 ns and reaches the steady-state

value around 16 ns for the solid cathode magnetron. The times for the structure with the cathode priming nearly the same, which are 9.5 ns and 15 ns, respectively. The transparent cathode magnetron starts to oscillate around 7.5 ns and reaches the peak value around 10.5 ns. Those voltage oscillation graphs show that the start-up time of the cathode priming structure is slightly better than the start-up time of the solid cathode structure while the transparent cathode structure have much better start-up time than both of them.

Another observation, which is the fourth one, is on the output power at the output slot. The graphs are in Figure 4.20. In the graphs output powers begin to form for the solid cathode magnetron, the solid cathode magnetron with cathode priming and the transparent cathode magnetron at 11 ns, 11 ns and 8 ns, respectively. In addition, power reaches the peak value at 17 ns, 16 ns and 12 ns, again respectively. The start-up performance of the transparent cathode magnetron is the best according to the power graphs and the cathode priming slightly improves the start-up time. Also, the output power of the transparent cathode magnetron is higher than the others and it is good for the applications which requires only high power. However, there is a ripple in the power of the transparent cathode magnetron at the steady-state. Therefore, the solid cathode magnetron would be more suitable for applications which requires stable output power.

The last observation plot is the current collected by the anode which is given in Figure 4.21. The start time of the anode current is 9.5 ns, 9 ns and 6.5 ns for the solid cathode, the cathode priming and the transparent cathode and they reach the peak value at 22 ns, 21 ns and 13.5 ns, respectively. The current plots are in accordance with the power plots in terms of the start-up improvements.

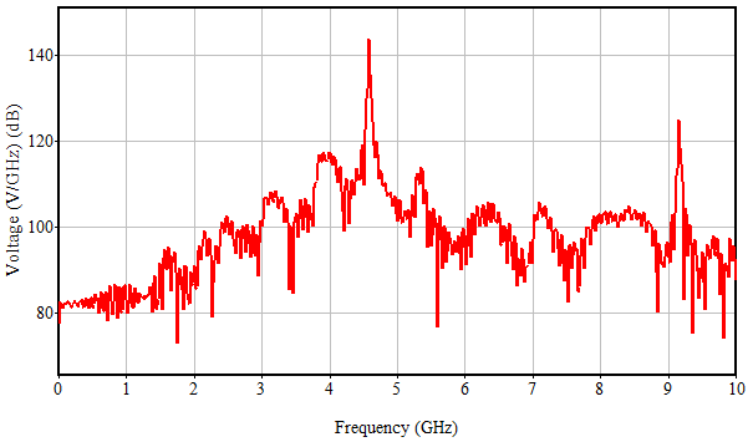

(a) Solid cathode

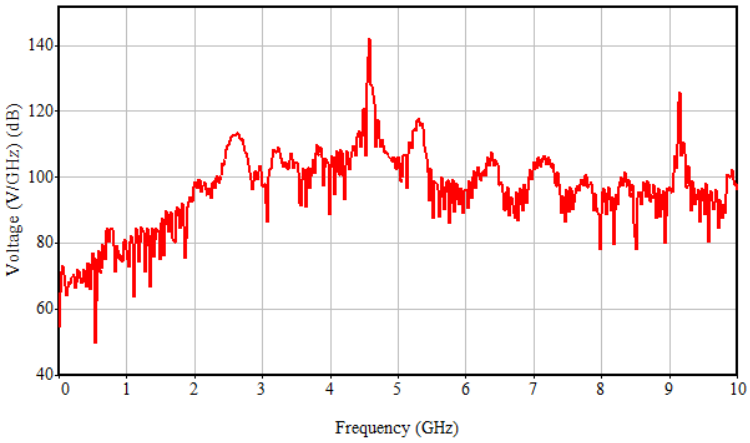

(b) Cathode priming

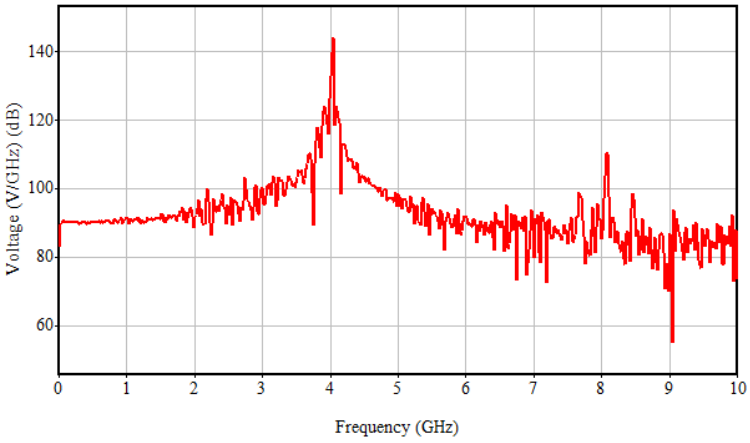

(c) Transparent cathode

Figure 4.17: Output spectrums of A6 magnetron with the solid cathode, the cathode priming and the transparent cathode in the simulations

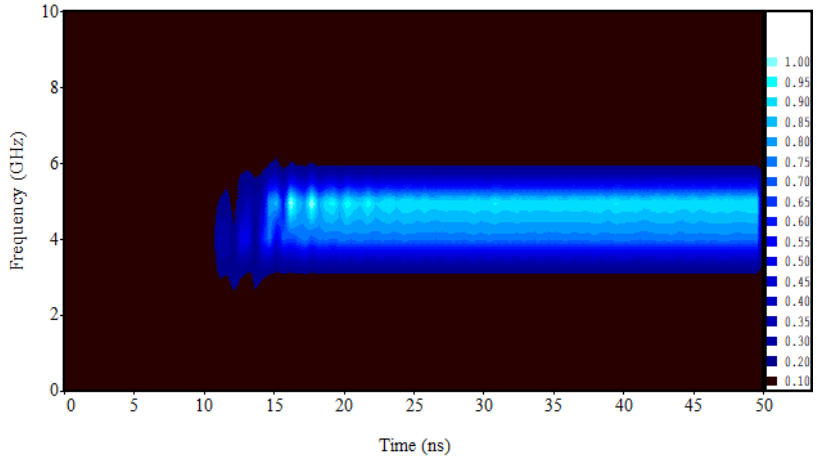

(a) Solid cathode

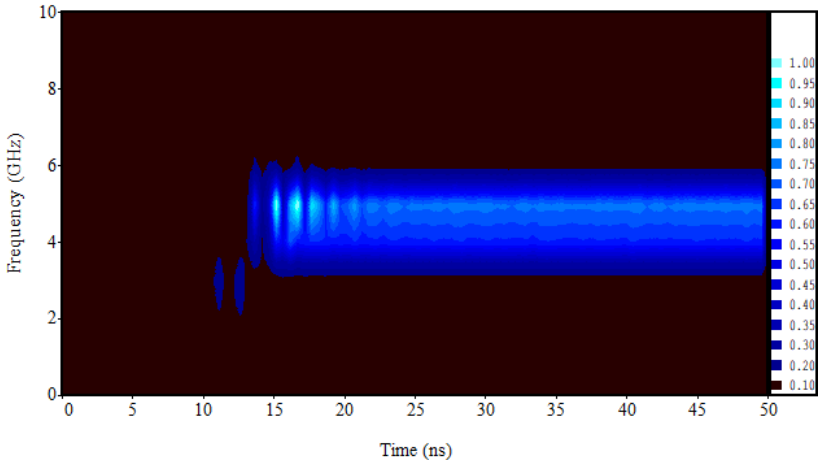

(b) Cathode priming

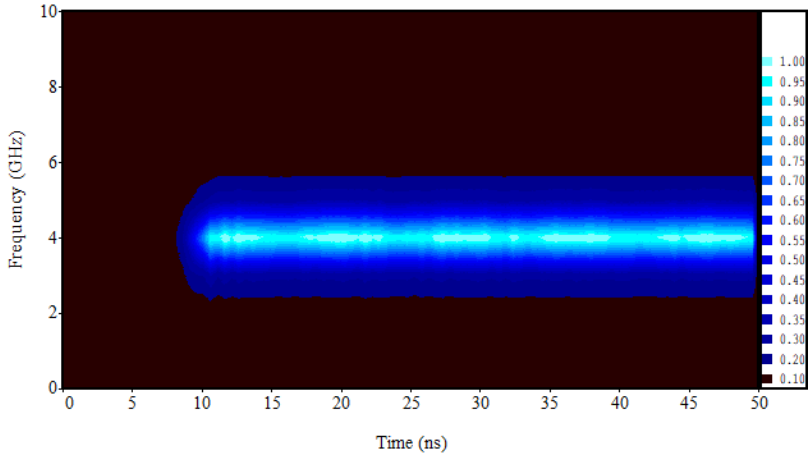

(c) Transparent cathode

Figure 4.18: Time-frequency spectrograms of A6 magnetron with the solid cathode, the cathode priming and the transparent cathode in the simulations

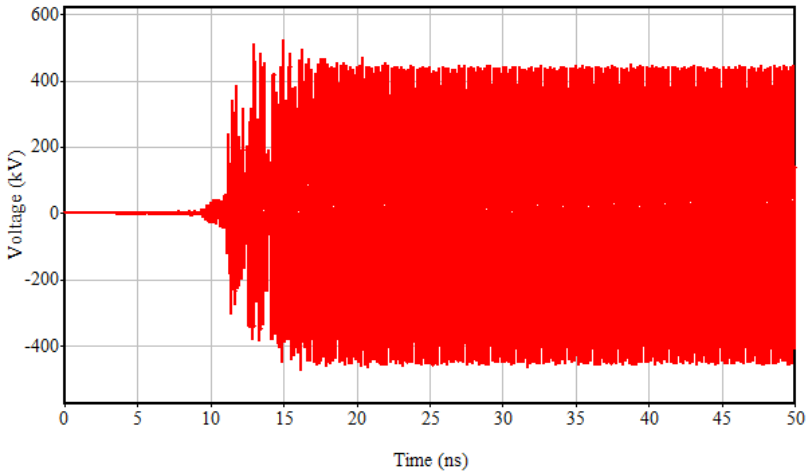

(a) Solid cathode

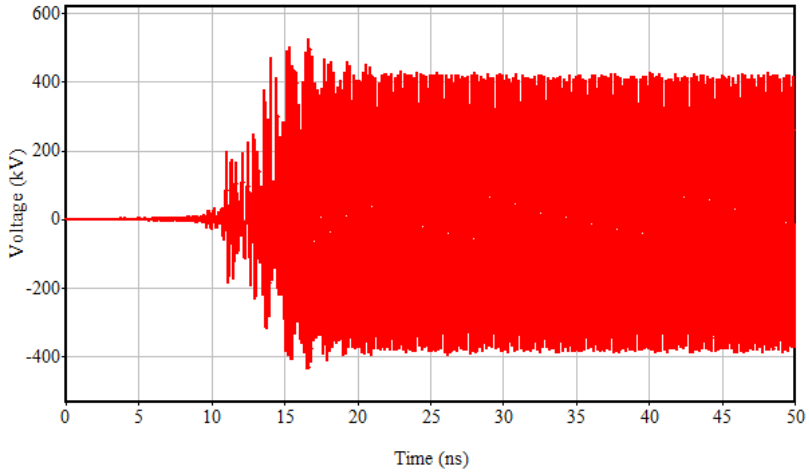

(b) Cathode priming

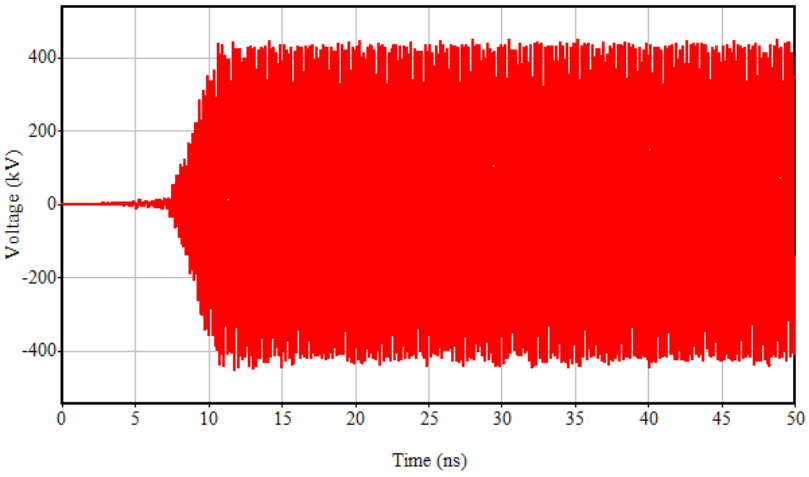

(c) Transparent cathode

Figure 4.19: Voltage oscillations at the output port of A6 magnetron with the solid cathode, the cathode priming and the transparent cathode in the simulations

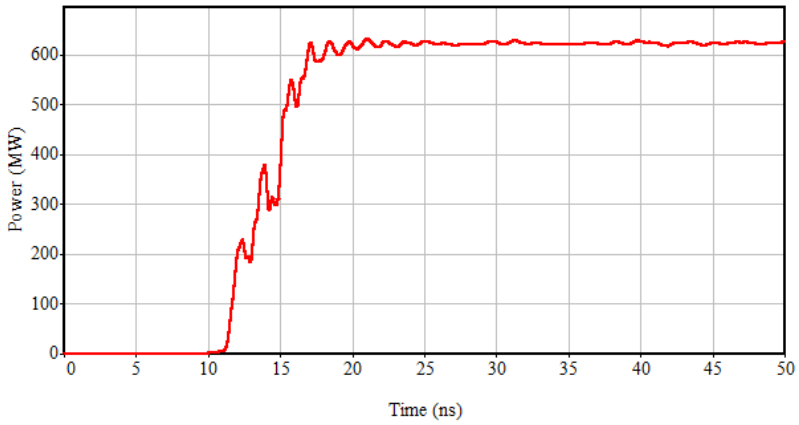

(a) Solid cathode

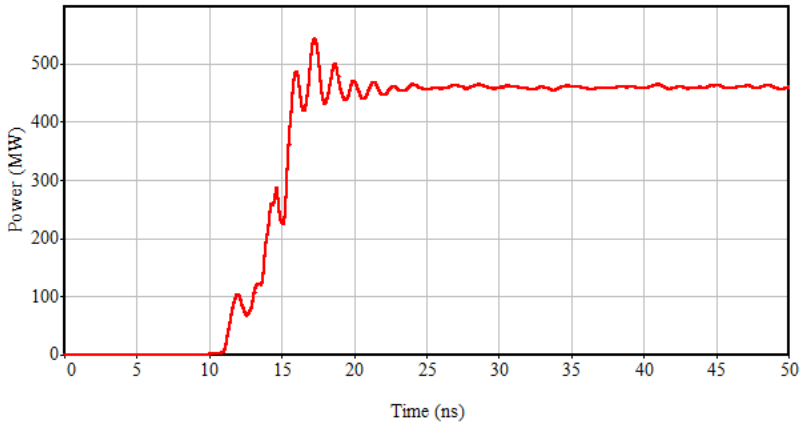

(b) Cathode priming

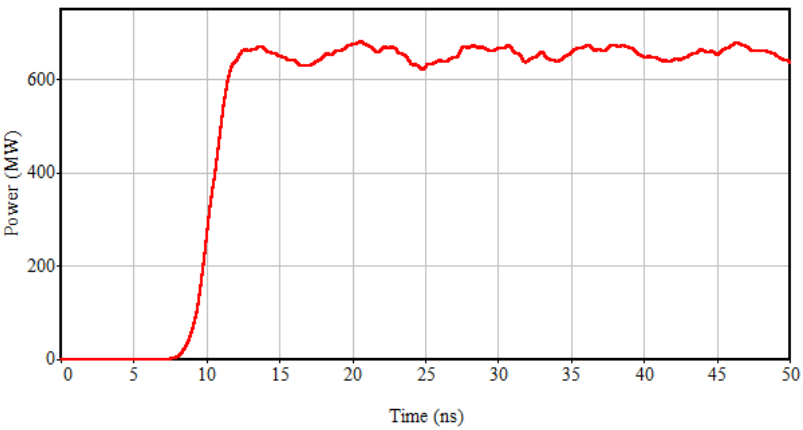

(c) Transparent cathode

Figure 4.20: Output power of A6 magnetron with the solid cathode, the cathode priming and the transparent cathode in the simulations

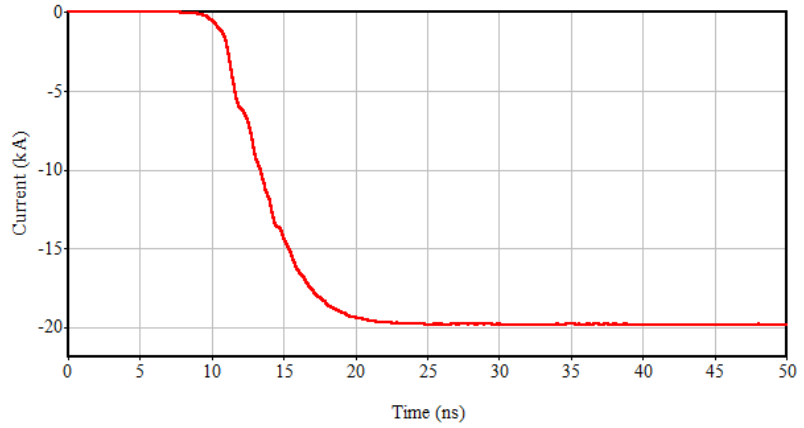

(a) Solid cathode

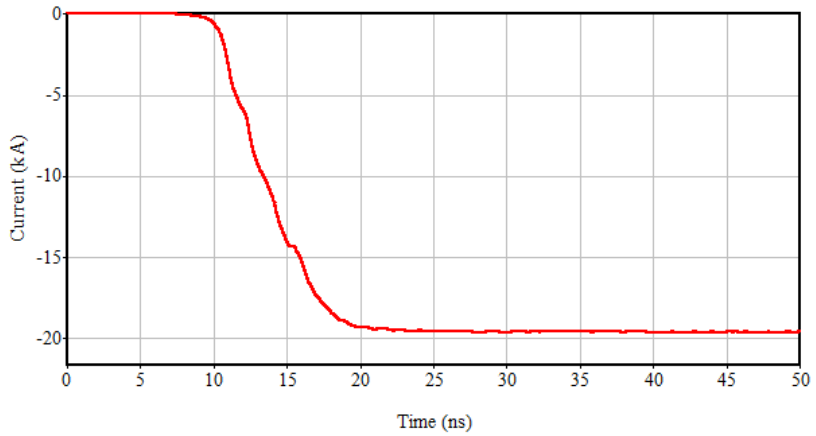

(b) Cathode priming

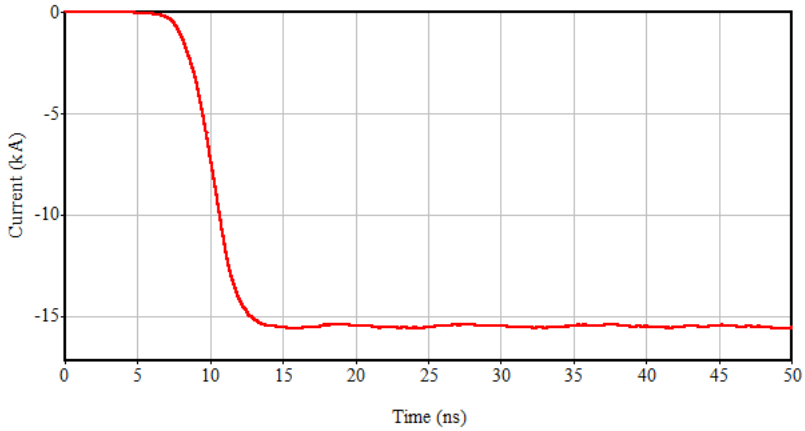

(c) Transparent cathode

Figure 4.21: Current collected by the anode of A6 magnetron with the solid cathode, the cathode priming and the transparent cathode in the simulations

In addition to the observations previously stated, the evolution of the azimuthal RF E-field was also investigated. The distributions of that E-field in the r-φ plane between 11 ns and 16 ns are given in Figure 4.22. In that figure, there is 180° phase difference between the red and the blue areas in terms of RF fields. At 11 ns, 12 ns and 13 ns, some cavities are shaded with the blue and the others are shaded with the red in the standard solid cathode magnetron. That corresponds to the different phases of the E-field in the different cavities meaning that the magnetron operates at the other mode than the desired 2π-mode operation. At 14 ns, the cavities of the standard solid cathode magnetron are all shaded with the blue and that shows the same phase at all the cavities implying the desired 2π-mode operation. At one step later, 15 ns, all cavities of the standard solid cathode magnetron are again at the same phase but this time it is 180° shifted with respect to the previous step because the cavities are red shaded. There is also the same situation at 16 ns step and that situation continues so on remaining of the runtime of the simulation. Therefore, it can be said for the standard solid cathode magnetron that its desired operation starts at 14 ns. Looking at the magnetron with the cathode priming in the same manner, there exists different mode of operations from 11 ns to 15 ns and the desired operation starts at 15 ns and keeps going. Investigating the times, the standard solid cathode magnetron and the one with the cathode priming have similar start-up times. On the other hand, the cavities of the transparent cathode are all at the same phase (blue shaded) at all time steps between 11 ns and 16 ns. That means the start of the desired 2π-mode operation is before the 11 ns and that is much before the start of the other type of magnetrons. There is no phase which corresponds to the red shaded area for the transparent cathode magnetron at those time steps. It is because the simulation do not catch that phase value due to the different output frequency of the transparent cathode magnetron than the other ones. The name transparent can also be understood by looking at the field distribution as the RF field strongly exists at the locations which are the interior of the cathode making it transparent to that field. In the view of the information obtained from the RF field investigation, it can be concluded that the transparent cathode magnetron starts much faster than the other types and the mode competition is suppressed in the transparent cathode magnetron.

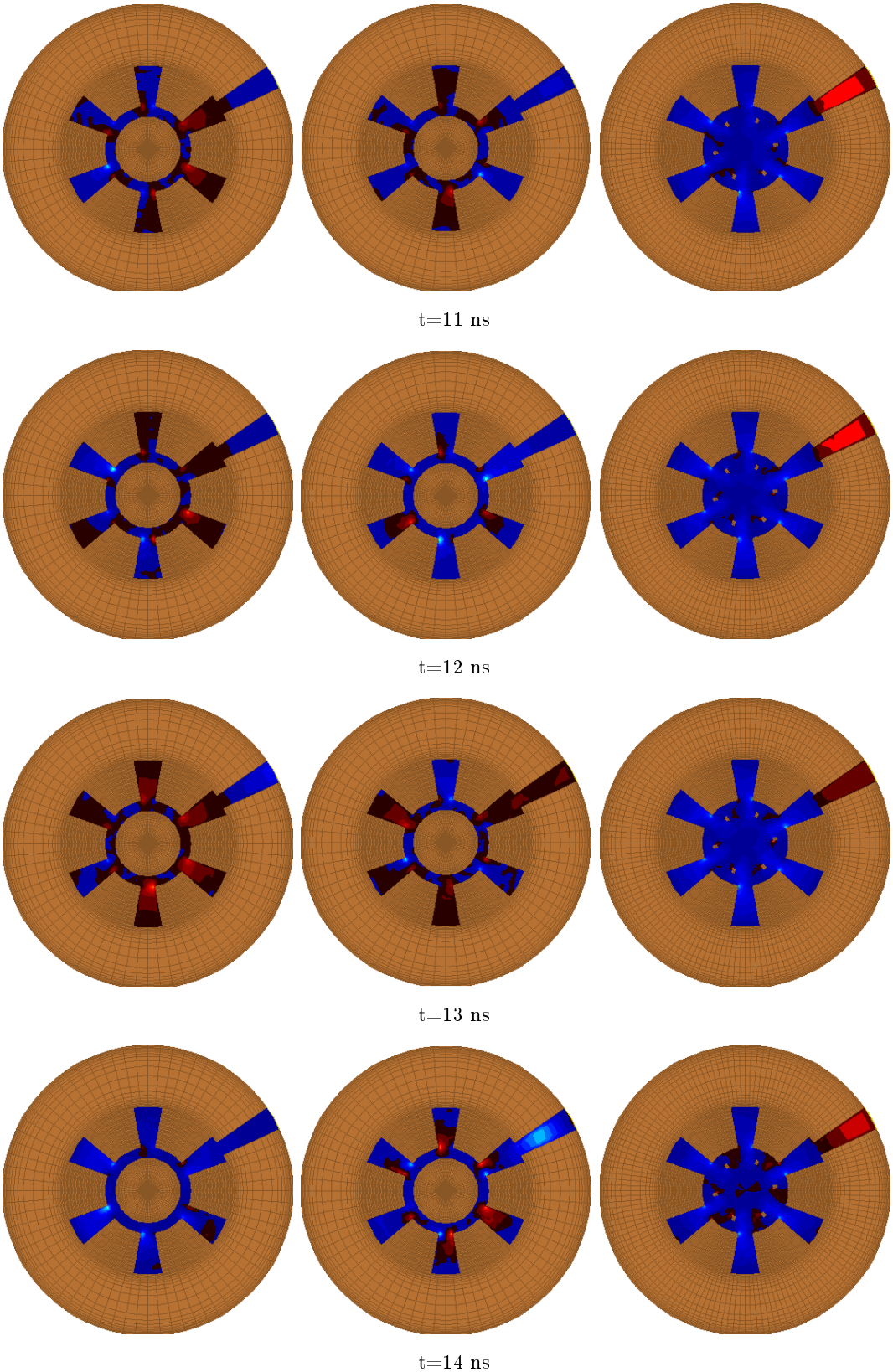

Figure 4.22: Evolution of the azimuthal E-field in the cavities of A6 magnetron with the solid cathode (left), the cathode priming (middle) and the transparent cathode (right) in the simulations

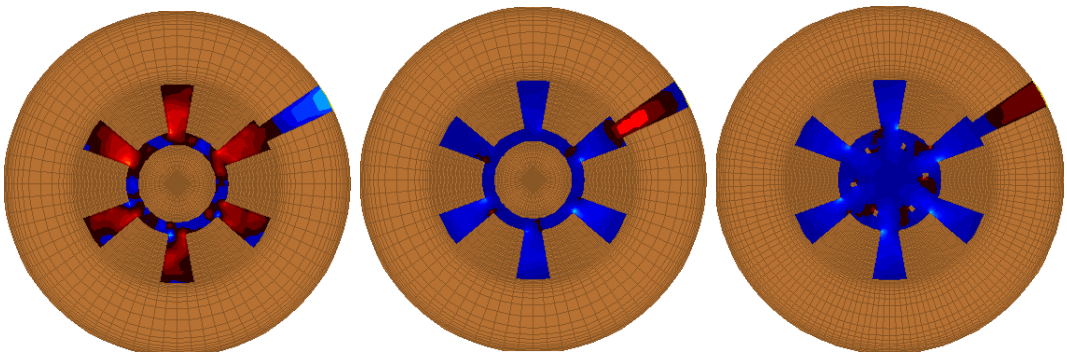

t=15 ns

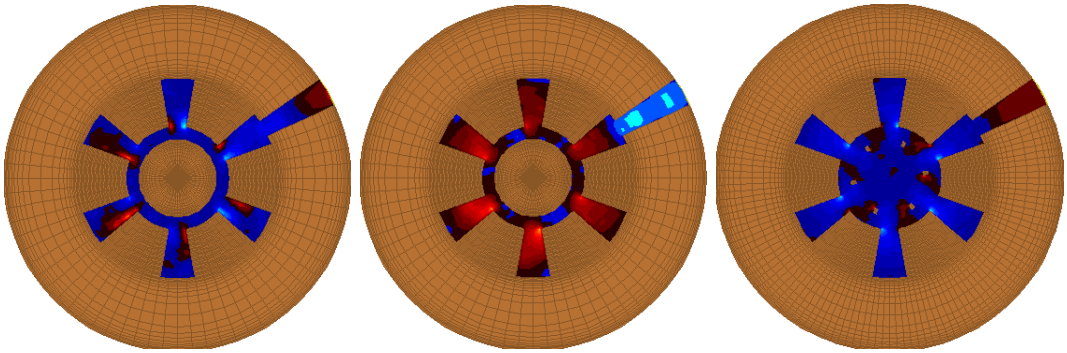

t=16 ns

Figure 4.22: Evolution of the azimuthal E-field in the cavities of A6 magnetron with the solid cathode (left), the cathode priming (middle) and the transparent cathode (right) in the simulations (cont.)

Another investigation was carried out on the particle distributions in the A-K gap. Those particle distributions at various times can be seen in Figure 4.23. In the standard solid cathode magnetron, there is only an electron cloud in the A-K gap until 12 ns and at that time, the first spoke structure is observed. However, the six-fold spoke structure of the desired mode (2π) forms at 16 ns and it continues to the end of the simulation. For the magnetron with the cathode priming, the situation is similar to the standard solid cathode magnetron. The first spoke structure is observed at 12 ns again but the six-fold spoke structure forms at 17 ns at this time. The transparent cathode magnetron shows spoke-like formation at 6 ns. However, the six-fold spoke structure forms at 8 ns and goes on till the end. Those particle plots show the significant speed at the start-up and suppression of the undesired modes in the transparent cathode magnetron while the other types have similar characteristics with each other.

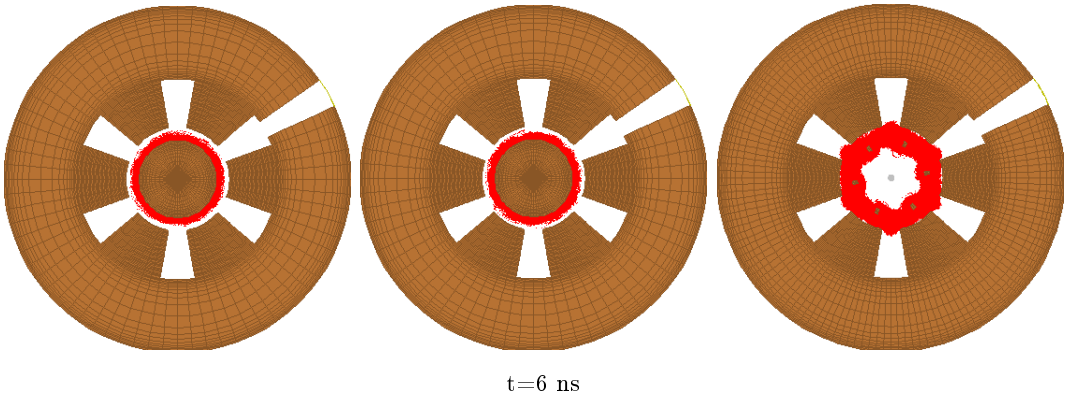

t=6 ns

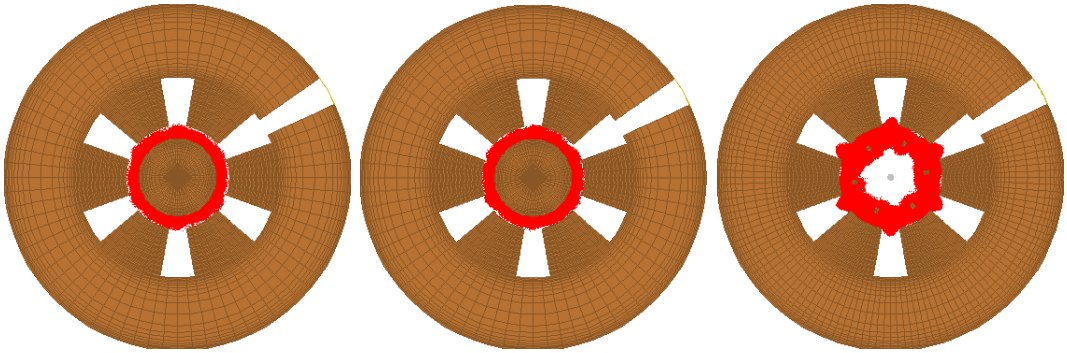

t=8 ns

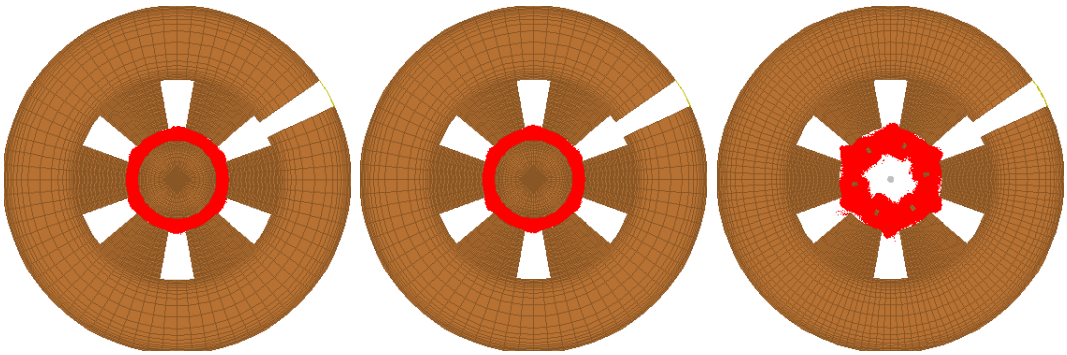

t=10 ns

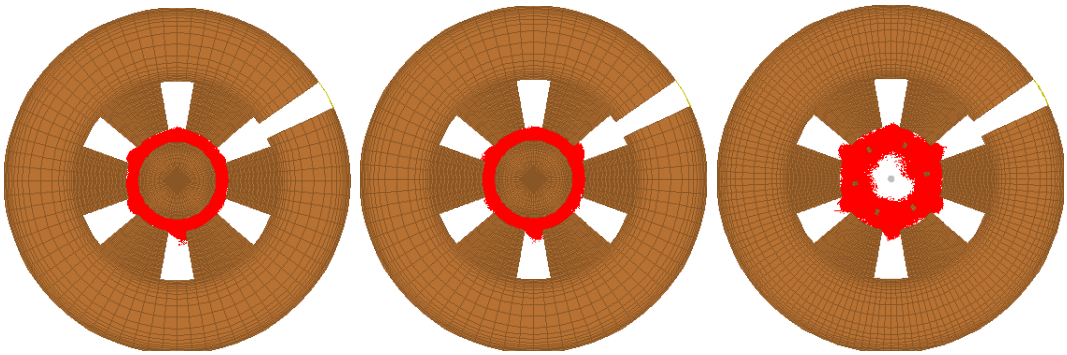

t=12 ns

Figure 4.23: Evolution of the particle traces in the A-K gap of A6 magnetron with the solid cathode (left), the cathode priming (middle) and the transparent cathode (right) in the simulations

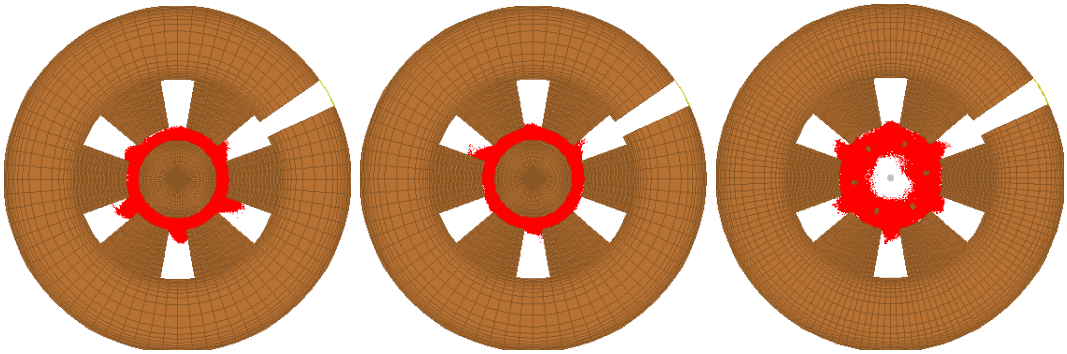

t=14 ns

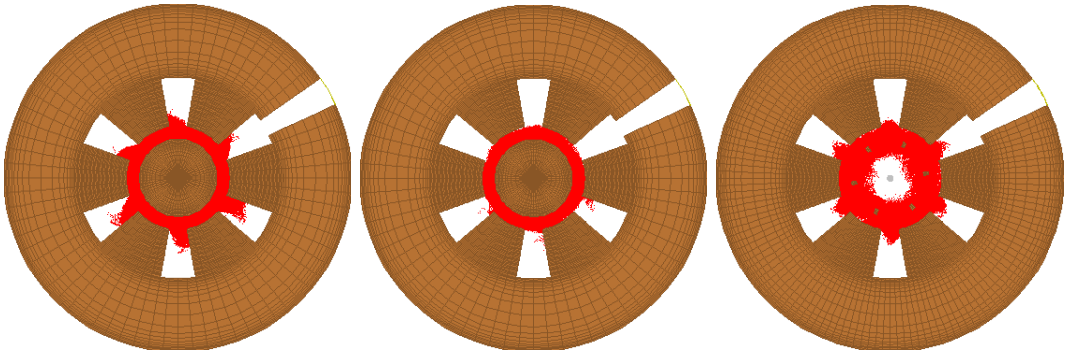

t=16 ns

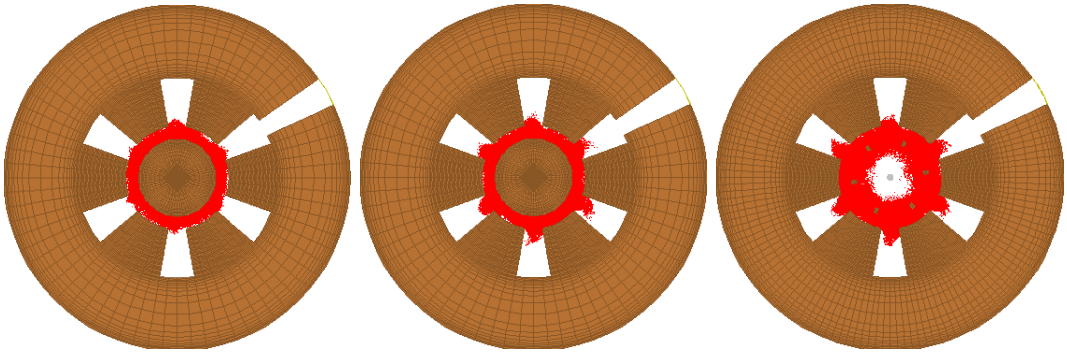

t=17 ns

Figure 4.23: Evolution of the particle traces in the A-K gap of A6 magnetron with the solid cathode (left), the cathode priming (middle) and the transparent cathode (right) in the simulations (cont.)

The simulations throughout this chapter compare the standard solid cathode magnetron, the solid cathode magnetron with the cathode priming and the transparent cathode magnetron. The results show significant improvement in the transparent cathode magnetron in terms of the start-up time and the mode competition issues. The other two types were observed as similar to each other in those aspects.

CHAPTER 5

INPUT LUMPED MODEL OF MAGNETRONS

5.1 Inductive Behavior of Magnetron Input

The transient behavior of the magnetron is the key point regarding the efforts for a faster start-up. Therefore, the behavior of the input current of the magnetron as a function of time was investigated during the simulations in order to understand the transient behavior. The data obtained from the simulations that give information about the input current is the collected electron current by the anode. That can be accepted as the input current from the DC supply because it closes the input circuit. The simulated time variation of the anode current in the solid cathode magnetron, whose model was given in the previous chapter, as time elapses is given in Figure 5.1.

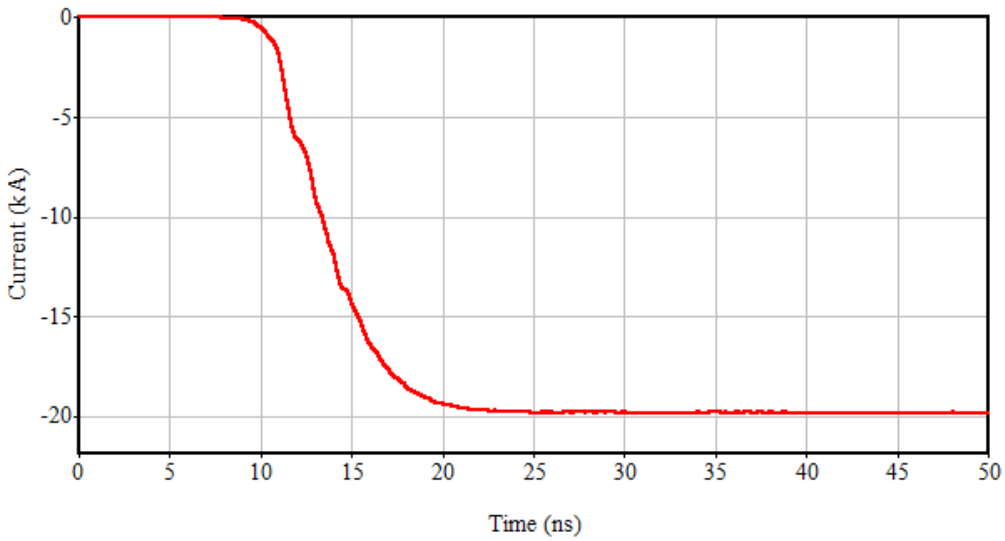

Figure 5.1: The simulated anode current of the solid cathode magnetron

Observing Figure 5.1, the current of the magnetron starts from zero at 0 ns when the input voltage waveform starts to be applied. After a time period, the electrons in the A-K gap begin to interact with the anode and the anode current starts to increase. That region is the one in which the transient behavior occurs. Finally, the anode current reaches the steady-state value. The point at which the current is stabilized is the one such that the start-up of the magnetron is completed and it begins to operate properly. That behavior of the current starting from zero and reaching the steady-state value after an exponential transient implies an inductive input for the magnetron. Decreasing the transient time of the input current means a faster start-up. Therefore, it is important to understand the reason behind that inductive behavior of the magnetron input and form a model for it within the scope of the attempts to get faster start-up.

5.2 Input Lumped Model

In this thesis, a lumped model as in Figure 5.2 is suggested for the magnetron input in order to understand the inductive behavior of the magnetron input. The suggested model of the magnetron input consists of an inductor and a resistor.

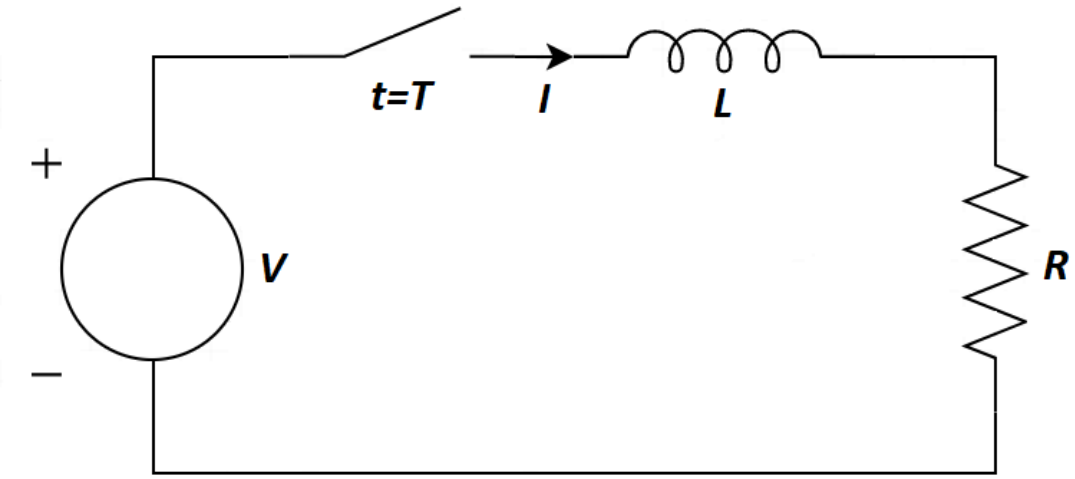

Figure 5.2: Suggested input lumped model of the magnetron

In Figure 5.1, the anode current (I in the model) starts at time T, represented by a switch closed at T in the model, and it increases exponentially with time before reaching the steady-state. An inductor shows that kind of transient current response. The resistor in the model stands for the steady-state behavior of the magnetron input. The voltage supply represents the input voltage waveform. However, it is assumed as constant, V, because at time T at which current starts (or switch is closed in the model), the applied voltage waveform in Figure 4.16 reaches to its maximum value.

The voltage across an inductor is related with the current through that inductor as,

$$V_L(t) = L\frac{dI_L(t)}{dt} \tag{5.1}$$

where V_L is the voltage across the inductor, I_L is the current through the inductor and L is the inductance. First, assuming $T = 0$ and using Kirchhoff's voltage law and substituting Equation (5.1), the differential Equation (5.2) for the current I in the model is found.

$$\frac{dI(t)}{dt} + \frac{R}{L}I(t) = \frac{V}{L} \tag{5.2}$$

The homogeneous solution of Equation (5.2) is $e^{-Rt/L}$ and the particular solution is V/R. Therefore, the current I is in the form,

$$I(t) = ke^{-\frac{t}{L/R}} + \frac{V}{R} \tag{5.3}$$

where k is a constant to be determined. In order to find k, Equation (5.4) is used since there is no anode current initially.

$$I(t = 0) = 0 \tag{5.4}$$

k is found to be $-V/R$. Substituting k in Equation (5.3) and including T, the current I is found as,

$$I(t) = \frac{V}{R}\left(1 - e^{-\frac{t-T}{\tau}}\right) \tag{5.5}$$

where τ is given by,

$$\tau = \frac{L}{R} \tag{5.6}$$

The values of parameters of the input lumped model in Figure 5.2 of the simulated solid cathode A6 magnetron is found by fitting Equation (5.5) to the

obtained current data from the simulations in Figure 5.1. The time, T, at which switch in the model is closed and the current starts, is chosen as 10.7 ns because the current before that time can be considered as negligible. Since the applied voltage waveform reaches its steady-state value (350 kV) before 10.7 ns, the constant V can be used in the model as 350 kV. On the current data in Figure 5.1, the steady-state value of the current is observed as 19.774 kA and dividing 350 kV by that current gives 17.7 Ω that corresponds to R in the suggested model. The fitting process is done in order to find L value in the model and the result is 57 nH. The real current data from the simulation and the curve calculated from the current in Equation (5.5) of the suggested model can be seen in Figure 5.3. In Figure 5.1, the particle current collected by the anode is negative. The simulation program puts negative sign in order to specify the sign of the charge of the particles collected and it is not related to the direction of the current flow due to those particles. Therefore, the magnitude of the current data from the simulations is used by omitting the negative sign in the fitting process as in Figure 5.3. As a conclusion, the input lumped model in Figure 5.2 for the solid A6 magnetron is suggested with the model parameters in Table 5.1.

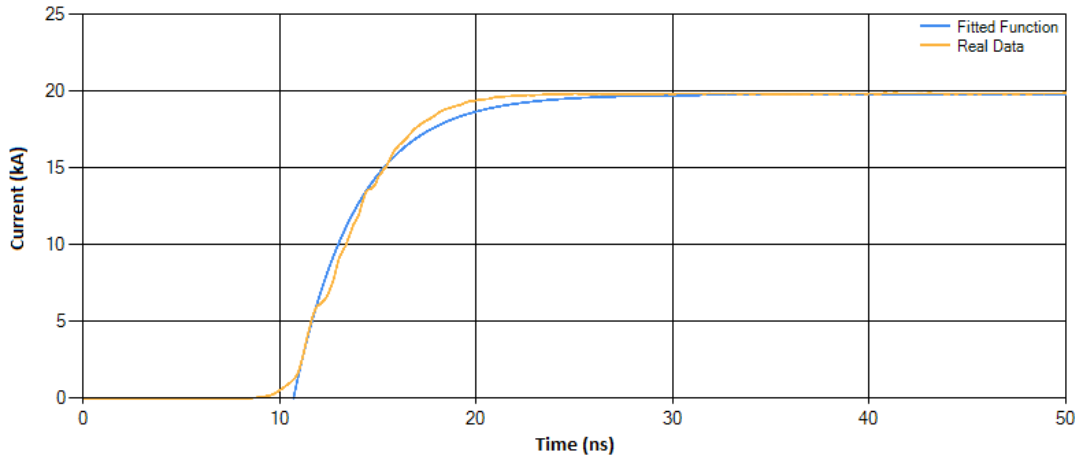

Figure 5.3: Real current data of the A6 magnetron from simulations and the fitted curve calculated from the suggested input model

Table5.1: Obtained parameters for suggested input lumped model of the solid cathode A6 magnetron

V (kV)	T (ns)	L (nH)	R (Ω)
350	10.7	57	17.7

5.3 Physical Implications

The inductance value in the input lumped model of the magnetron can be interpreted physically with two different suggestions. One of them considers the electron spokes in the interaction region as windings of a coil and the other one considers them as straight wires. This section gives an explanation of those two suggestions.

5.3.1 Coil Inductance Suggestion

While forming spokes in the interaction region, the electrons follow a path like in Figure 5.4. They rotate around the cathode forming an azimuthal modu-

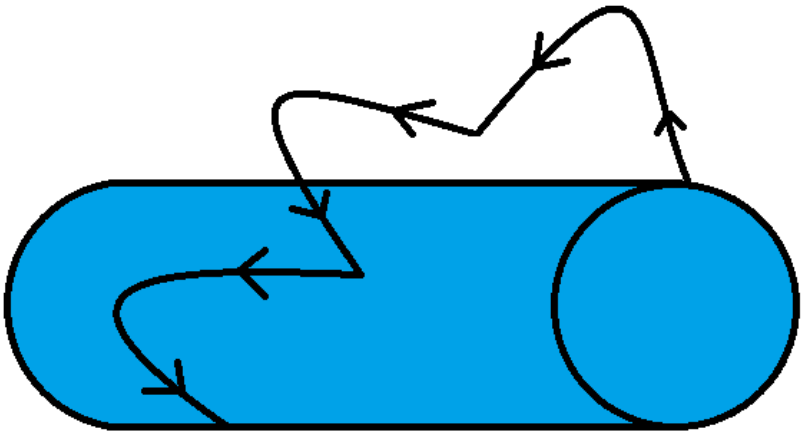

Figure 5.4: Electron path in the interaction region while forming spokes

lation and they also drift axially. That rotation forms loop-like paths. Each spoke can be considered as a wire forming a loop and since there exists an axial magnetic field in the interaction space, current due to the electron rotation can

be considered as an induced current. Therefore, each spoke can be considered as a winding of a coil having vacuum inside. In that configuration windings are not placed along a cylinder axially, they also have a rotation azimuthally. However, since there is the same vacuum inside each loop and the same uniform magnetic field and the current flow through each spoke continuously like a single wire, the assumption of the spokes as the windings of a coil is plausible.
The inductance of a coil is calculated by [41],

$$L = \mu \frac{N^2 A}{l} \tag{5.7}$$

where L is the coil inductance, μ is the permeability of the core, N is the number of windings, A is the area of the core and l is the length of the core.
The inductance of the input lumped model of the magnetron can be calculated using the coil inductance formula assuming each spoke in the interaction region as a winding of a coil. In the case of the A6 magnetron, which is the magnetron investigated throughout the thesis, the number of windings (N) can be taken as 6, that is the number of spokes. Since the interaction space is vacuum, the permeability of the core (μ) is the permeability of the free space which is $4\pi 10^{-7}$ H/m. The length of the core (l) is 7.2 cm which is the axial length of the A6 magnetron. The area is taken as the area of a spoke. That area can be seen in Figure 5.5. In that figure, although one side is an arc that

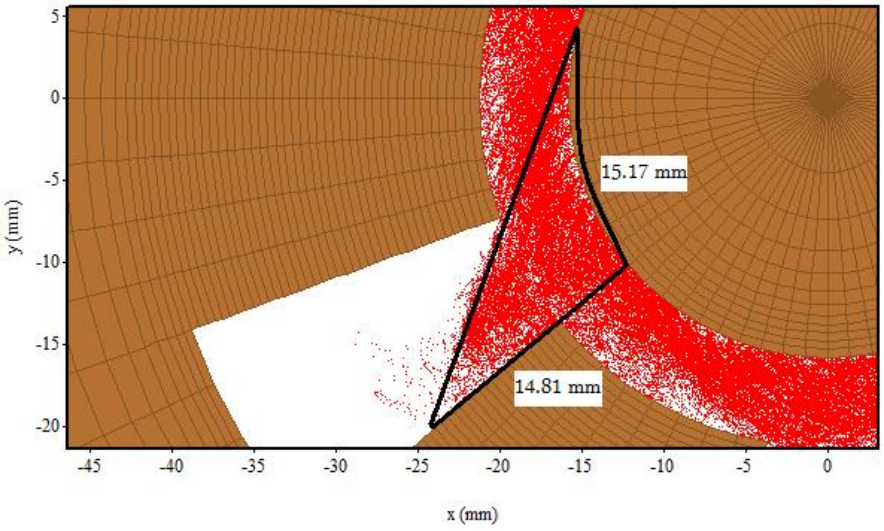

Figure 5.5: Area of a spoke in the interaction region

shape can be considered as a right triangle and the area can be calculated by multiplying the lengths of both sides and dividing by two. The area is calculated as 112.33 mm^2. That calculated area in the figure is just indicative and it is chosen by an engineering insight with a one-time trial. However, the area can be chosen with different approaches. Substituting all values in Equation (5.7), the inductance value is found as 70.58 nH. That value and the calculated value of the input lumped model in the previous section, which is 57 nH, are comparable within the same order of magnitude. As a result, the inductive behavior of the magnetron input model might be explained with the coil inductance suggestion and the related parameters, that are obtained for the A6 magnetron from the simulations, are as in Table 5.2.

Table5.2: Calculated parameters for coil inductance approach of the solid cathode A6 magnetron

L (nH)	μ (H/m)	N	A (mm^2)	l (mm)
70.58	$4\pi 10^{-7}$	6	112.33	72

5.3.2 Wire Inductance Suggestion

The path which the electrons follow in the interaction space was given in Figure 5.4 in the previous subsection. In that subsection, the spokes are considered as windings of a coil. Since the windings are formed from a continuous wire, each spoke can be considered as a cylindrical wire. Therefore, in this subsection, the spokes are considered as just wires instead of windings of a coil and they are considered to be joined each other in series. As a result, in the wire inductance suggestion, the inductance of the input lumped model is calculated by finding the inductance of a spoke with the assumption of a cylindrical wire and multiplying it by the number of the spokes because the spokes are assumed to be joined in series. In order to find the inductance of a spoke, the self-inductance formula for a wire is [42],

$$L = 2l\left[ln\left[\left(\frac{2l}{D}\right)\left(1+\sqrt{1+\left(\frac{D}{2l}\right)^2}\right)\right] - \sqrt{1+\left(\frac{D}{2l}\right)^2} + \frac{\mu_r}{4} + \left(\frac{D}{2l}\right)\right] \quad (5.8)$$

where L is the wire inductance, l is the length of the wire (in cm), D is the diameter of the wire (in cm) and μ_r is the relative permeability.
The length and the diameter of a wire related to a spoke in the interaction region of the A6 magnetron are as in Figure 5.6. The lines passing through

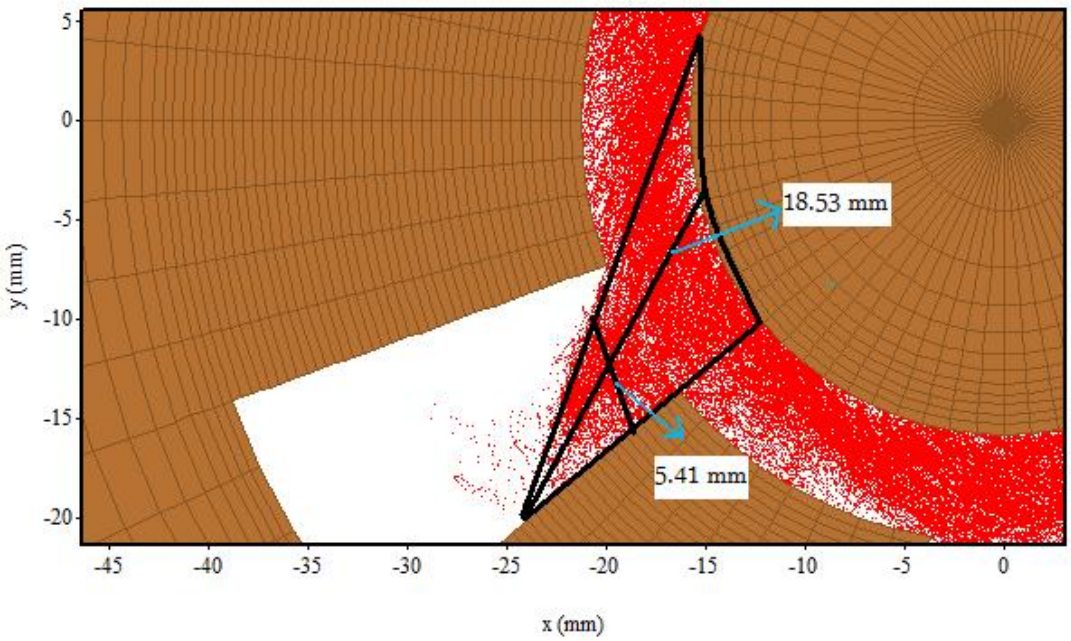

Figure 5.6: Length and diameter of a spoke in the interaction region

the center points of the triangle forming the spoke are used in order to find the length and the diameter parameters of the wire. In that way, the length and the diameter are found to be 18.53 mm and 5.41 mm, respectively. The approach used in order to choose the lengths depends on an intuition and one-time trial. On the other hand, different approaches can be used in order to determine those lengths. Substituting the values in the Equation (5.8) while taking μ_r=1 (vacuum), the inductance of a spoke is found as 7.44 nH. Since there are six spokes in the A6 magnetron, the total inductance is 44.64 nH. That value and the calculated value of the input lumped model in the previous section, which is 57 nH, are comparable within the same order of magnitude. As a result, the inductive behavior of the magnetron input model might be explained with the wire inductance suggestion.

5.4 Comments on Results

In this chapter, an input lumped model is suggested for a magnetron. That model differs from the other lumped models in the literature because it treats the DC input port instead of the RF output port and the cavities. The model is formed with the belief of an inductive input because of the time variation of the anode current. The curve fitting results and the calculations from two different physical suggestions are comparable within the same order of magnitude. That supports the inductive input belief and the suggested model. However, more simulations and measurements could be done in order to verify those suggestions. The suggested model is a start point. In the future studies, that model can be improved by adding the effects of the input supply and more accurate results can be found. Also, the physical suggestions can be improved and verified with more observations on magnetrons.

CHAPTER 6

CONCLUSION

Today, magnetrons are one of the HPM sources of which studies are carried out in order to improve their designs. The higher output power levels have already been reached by the invention of relativistic magnetrons. However, those magnetrons have one kind of drawback and that is pulse-shortening issue. That problem causes the reduction of the radiated energy in spite of the higher level of output power. Therefore, the focus of the studies on relativistic magnetrons is to solve the pulse shortening issue. One solution is to reduce the start-up time and by that way, to increase the energy per pulse, or average power. In the view of that information, this thesis investigates the ways to hasten the start of magnetrons, especially relativistic ones. In Chapter 2, the magnetron structure, the parameters to be considered in the design process and the parameters to be evaluated after design are mentioned. In Chapter 3, the literature search results for the methods that hasten the start-up of magnetrons are given. Those include the priming techniques, that are cathode priming, magnetic priming, electric priming and RF priming, and the transparent cathode magnetron. In Chapter 4, simulations for the fast start-up techniques are presented. Those simulations were done in MAGIC PIC simulation environment in order to compare the start-up times of three modified cathode type used in relativistic A6 magnetron which are the standard solid cathode, the solid cathode with the cathode priming and the transparent cathode. The simulations showed improvement of the start-up time in the transparent cathode as compared to other ones by investigating the transient behavior of the output power and the anode current and observing the particle and field distribution in the interaction space. In Chapter 5, an input lumped model for magnetrons are suggested in order to explain the transient

behavior of magnetrons at the start-up. The value of the inductance, which is responsible for the transient behavior of the magnetron, in the model for A6 magnetron is calculated from the results of the simulations carried out in the previous chapter and a physical explanation for why that kind of inductive behavior exists in magnetrons is given using two suggestions. One of them treats the electron spokes in the interaction space as a coil and the other one treats as a straight wire. The inductance values obtained from both suggestions and the calculated inductance value from the input lumped model are within the same order of magnitude. Therefore, those two suggestions might explain the inductive behavior of the magnetron input. However, they are just suggestions and more simulations and measurements should be done as a future work in order to understand whether they are sufficient explanations. In conclusion, that model gave a start towards the explanation of the start-up transient behavior of magnetrons and that model can be improved and linked to the design parameters of magnetrons in detail enabling the faster start-up magnetrons in the future works.

REFERENCES

[1] M. I. Skolnik, *Introduction to Radar Systems*. New York, NY: McGraw-Hill, 2001.

[2] G. B. Collins, *Microwave Magnetrons*. New York: McGraw-Hill, 1948.

[3] C. Wolff, "Magnetron," [Online]. Available: `http://www.radartutorial.eu/08.transmitters/Magnetron.en.html`. [Accessed Jan 28, 2018].

[4] A. S. Gilmour, *Klystrons, Travelling Wave Tubes, Magnetrons, Cross-field Amplifiers, and Gyrotrons*. Boston, MA: Artech House, Inc, 2011.

[5] S. E. Tsimring, *Electron Beams and Microwave Vacuum Electronics*. John Wiley & Sons, 2006.

[6] J. Benford, J. A. Swegle, and E. Schamiloglu, *High Power Microwaves*. Boca Raton, FL: CRC Press, 2016.

[7] R. B. Miller, *An Introduction to the Physics of Intense Charged Particle Beams*. Springer Science & Business Media, 2012.

[8] A. W. Hull, "The effect of a uniform magnetic field on the motion of electrons between coaxial cylinders," *Phys. Rev.*, vol. 18, no. 1, pp. 31–57, Jul. 1921.

[9] H. Yagi, "Beam transmission of ultra short waves," *Proc. Institute of Radio Engineers*, vol. 16, no. 6, pp. 715–740, Jun. 1928.

[10] K. Posthumus, "Oscillations in a split anode magnetron," *Wireless Engineer*, vol. 12, no. 138, pp. 126–132, Mar. 1935.

[11] A. L. Samuel, "Electron discharge device," US Patent 2,063,342, 8 Dec., 1936.

[12] H. E. Hollmann, "Magnetron," US Patent 2,123,728, 12 Jul., 1938.

[13] N. F. Alekseev, D. D. Malairov, and I. B. Bensen, "Generation of high-power oscillations with a magnetron in the centimeter band," *Proc. IRE*, vol. 32, no. 3, pp. 136–139, Mar. 1944.

[14] H. A. H. Boot and J. T. Randall, "The cavity magnetron," *Journal of the Institution of Electrical Engineers - Part IIIA: Radiolocation*, vol. 93, no. 5, pp. 928–938, 1946.

[15] E. C. S. Megaw, "The high-power pulsed magnetron: a review of early developments," *Journal of the Institution of Electrical Engineers - Part IIIA: Radiolocation*, vol. 93, no. 5, pp. 977–984, 1946.

[16] J. T. Randall and H. A. H. Boot, "High-frequency electrical oscillator," US Patent 2,542,966, 20 Feb., 1951.

[17] J. T. Randall and H. A. H. Boot, "Magnetron," US Patent 2,648,028, 4 Aug., 1953.

[18] G. Bekefi and T. J. Orzechowski, "Giant microwave bursts emitted from a field-emission, relativistic-electron-beam magnetron," *Physical Review Letters*, vol. 37, no. 6, pp. 379–382, Aug. 1976.

[19] A. Rosenberg, "Magnetron construction particularly useful as a relativistic magnetron," US Patent 5,552,672, 3 Sep., 1996.

[20] J. Benford, "History and future of the relativistic magnetron," in *2010 Int. Conf. Origins and Evolution of the Cavity Magnetron*, pp. 40–45, Apr. 2010.

[21] J. Benford and G. Benford, "Survey of pulse shortening in high-power microwave sources," *IEEE Trans. Plasma Sci.*, vol. 25, no. 2, pp. 311–317, Apr. 1997.

[22] D. Price, J. S. Levine, and J. N. Benford, "Diode plasma effects on the microwave pulse length from relativistic magnetrons," *IEEE Trans. Plasma Sci.*, vol. 26, no. 3, pp. 348–353, Jun. 1998.

[23] W. M. White, R. M. Gilgenbach, M. C. Jones, V. B. Neculaes, Y. Y. Lau, P. Pengvanich, N. M. C. Jordan, B. W. Hoff, R. Edgar, T. A. Spencer, and D. Price, "Radio frequency priming of a long-pulse relativistic magnetron," *IEEE Trans. Plasma Sci.*, vol. 34, no. 3, pp. 627–634, Jun. 2006.

[24] A. D. Andreev and K. J. Hendricks, "Icepic simulation of a strapped nonrelativistic high-power uhf magnetron with a transparent cathode operating in the explosive electron emission mode," *IEEE Trans. Plasma Sci.*, vol. 40, no. 10, pp. 2535–2547, Oct. 2012.

[25] H. L. Bosman, M. I. Fuks, S. Prasad, and E. Schamiloglu, "Improvement of the output characteristics of magnetrons using the transparent cathode," *IEEE Trans. Plasma Sci.*, vol. 34, no. 3, pp. 606–619, Jun. 2006.

[26] J. I. Kim, S. G. Jeon, Y. S. Jin, G. J. Kim, and C. H. Shon, "Three-dimensional particle-in-cell simulation of fast oscillation startup in strapped magnetron using electrically primed electrons," *Jpn. J. Appl. Phys.*, vol. 46, no. 10A, pp. 6853–6856, Oct. 2007.

[27] M. Fuks and E. Schamiloglu, "Magnetron having a transparent cathode and related methods of generating high power microwaves." US Patent 8,324,811, 4 Dec., 2012.

[28] W. Yang, Z. Dong, Y. Yang, and Y. Dong, "Numerical investigation of the relativistic magnetron using a novel semitransparent cathode," *IEEE Trans. Plasma Sci.*, vol. 42, no. 11, pp. 3458–3464, Nov. 2014.

[29] M. C. Jones, V. B. Neculaes, Y. Y. Lau, R. M. Gilgenbach, and W. M. White, "Cathode priming of a relativistic magnetron," *Appl. Phys. Lett.*, vol. 85, no. 26, pp. 6332–6334, Dec. 2004.

[30] R. M. Gilgenbach, M. C. Jones, V. B. Neculaes, Y. Y. Lau, W. M. White, N. M. Jordan, B. W. Hoff, R. C. Edgar, P. Pengvanich, and Y. Hidaka, "Cathode priming of magnetrons for rapid startup and mode-locking," in *2005 Joint 30th Int. Conf. Infrared and Millimeter Waves and 13th Int. Conf. Terahertz Electronics*, vol. 2, pp. 535–536, Sep. 2005.

[31] M. C. Jones, V. B. Neculaes, W. M. White, Y. Y. Lau, R. M. Gilgenbach, J. W. Luginsland, P. Pengvanich, N. M. Jordan, Y. Hidaka, and H. L. Bosman, "Simulations of magnetic priming in a relativistic magnetron," *IEEE Trans. Electron Devices*, vol. 52, no. 5, pp. 858–863, May 2005.

[32] V. B. Neculaes, M. C. Jones, R. M. Gilgenbach, Y. Y. Lau, J. W. Luginsland, B. W. Hoff, W. M. White, N. M. Jordan, P. Pengvanich, Y. Hidaka, and H. L. Bosman, "Magnetic priming effects on noise, startup, and mode competition in magnetrons," *IEEE Trans. Plasma Sci.*, vol. 33, no. 1, pp. 94–102, Feb. 2005.

[33] S. Maurya, V. V. P. Singh, and P. K. Jain, "Three-dimensional particle-in-cell simulation of fast oscillation startup and efficiency improvement in a relativistic magnetron with electric priming," *IEEE Trans. Plasma Sci.*, vol. 40, no. 10, pp. 2686–2692, Oct. 2012.

[34] S. Maurya, V. P. Singh, and P. K. Jain, "Relativistic magnetron priming by loading the resonators through dielectric rods," *IEEE Trans. Plasma Sci.*, vol. 41, no. 12, pp. 3619–3623, Dec. 2013.

[35] E. Schamiloglu and M. I. Fuks, "The transparent cathode: Rejuvenator of magnetrons and inspiration for new RF sources," in *2009 IET Conf. High Power RF Technologies*, pp. 1–5, Feb. 2009.

[36] S. Prasad, M. Roybal, C. J. Buchenauer, K. Prestwich, M. Fuks, and E. Schamiloglu, "Experimental verification of the advantages of the transparent cathode in a short-pulse magnetron," in *2009 IEEE Pulsed Power Conf.*, pp. 81–85, Jun. 2009.

[37] M. Fuks, S. Prasad, and E. Schamiloglu, "Increased efficiency and faster turn-on in magnetrons using the transparent cathode," in *2010 Int. Conf. Origins and Evolution of the Cavity Magnetron*, pp. 76–81, Apr. 2010.

[38] B. Goplen, L. Ludeking, D. Smithe, and G. Warren, "User-configurable magic for electromagnetic pic calculations," *Comput. Phys. Commun.*, vol. 87, no. 1, pp. 54–86, May 1995.

[39] L. Ludeking, A. Woods, and L. Cavey, "Magic 3.2.0 help manual," Orbital ATK, VA. [Online]. Available: `https://www.orbitalatk.com/magic/FormsPDF/MagicManual.pdf`. [Accessed Feb 18, 2018].

[40] A. Palevsky and G. Bekefi, "Microwave emission from pulsed, relativistic e-beam diodes. ii: The multiresonator magnetron," MIT Plasma Science and Fusion Center, Cambridge, MA, PFC/JA-78-5, Jul. 1978.

[41] "Inductance of a coil," [Online]. Available: `https://www.electronics-tutorials.ws/inductor/inductance.html`. [Accessed Apr 4, 2018].

[42] "Wire self inductance calculator," [Online]. Available: `https://www.allaboutcircuits.com/tools/wire-self-inductance-calculator`. [Accessed Apr 4, 2018].